Fringing Electric Field Sensors for the Detection of Incipient Thermal Damage in Composite Materials

Jeffrey Thomas

A thesis

submitted in partial fulfillment of the

requirements for the degree of

Master of Science in Electrical Engineering

University of Washington
2021

Committee:

Alexander V. Mamishev

Rania Hussein

Santosh Devasia

Program Authorized to Offer Degree:

Electrical and Computer Engineering

University of Washington

Abstract

Fringing Electric Field Sensors for the Detection of Incipient Thermal Damage in Composite Materials

Jeffrey Thomas

Chair of the Supervisory Committee:

Alexander Mamishev

Department of Electrical and Computer Engineering

Commercial and military aviation has rapidly adopted the use of carbon composites due to their structural strength and light weight in comparison to metal alloys. As with metal aircraft, composite aircraft require regular inspection to maintain flight worthiness and safety for passengers and crew, however, thermal damage in composites is not detectable using conventional non-destructive evaluation (NDE) methods until after the material loses as much as 50% of its mechanical strength. Additionally, many NDE methods are expensive or severely limited by depth, resolution, or access to both sides of the material under Test (MUT). Dielectric spectroscopy combined with electric field sensors presents the possibility of a more effective means of identifying thermal damage in composite materials and enhance existing composite NDE methods. The goal of this thesis is to evaluate the effectiveness of detecting non-visible incipient thermal damage in composites using Fringing Electric Field (FEF) sensors and dielectric spectroscopy. We designed and implemented two sensors developed using established parameters for electric field sensors and analyzed sensor response using custom algorithms developed in MATLAB. Six

aerospace composite samples, one undamaged and five exposed to temperatures ranging from 450°F to 626°F, were used to characterize the sensor response. An additional five composite samples with unknown thermal damage were measured for blind identification and validation. Spectroscopic FEF sensor measurements demonstrated thermal correlation above 70 kHz in calibrated gain sensor response with a low resolution of 0.03 dBV across all samples. Intra-sample overlap in sensor gain response resulted in the successful identification of only three of the five blind composite samples. Variation in sample measurements is attributed to the limited thermal resolution of the sensor and a standard deviation of individual sample measurements exceeding 8 percent due to sample geometry and physical damage. This thesis demonstrates a partial correlation between thermal damage in aerospace composites and their dielectric response via electric field sensor measurements above 70 kHz. With additional development, dielectroscopy with FEF sensors presents the potential to supplement and improve upon existing aerospace composite NDE technologies.

TABLE OF CONTENTS

LIST OF FIGURES

LIST OF TABLES

ACKNOWLEDGEMENTS

Firstly, I would like to express my sincere gratitude to my advisor Prof. Alexander Mamishev for his mentorship and support of my Master's study and related research for his patience, encouragement, and knowledge. I would also like to thank the USAF, The Boeing Company, Brian Flynn of GT Engineering, and Dr. Ryan Toivola for advice, support, funding, and resources. Finally, I would like to thank Dr. Rania Hussein for her support, encouragement, and advice in completing this thesis.

Chapter 1. Introduction

The goal of this thesis is to determine the capability of FEF sensors as a non-destructive measurement technique to detect non-visible, incipient thermal damage in BMI carbon composites for use in aerospace applications. The approach is two-fold: to use wideband dielectric spectroscopy to identify the relaxation response of known thermally damaged BMI composite samples and to use calibrated measurements to detect and identify the magnitude of incipient thermal damage in otherwise unknown composite samples. By correlating the capacitance, gain, and phase measurements to the temperature exposure of known samples a transfer function relating the sensor response to the temperature exposure can be obtained.

1.1 Introduction to FEF Sensors

Conventional capacitors utilize dielectric materials to enhance their performance and electrical properties by exploiting the relationship between capacitance and the dielectric properties of the material used. Similarly, FEF sensors utilize these dielectric principles to correlate the voltage, current, and capacitance across the sensor to the physical, structural, geometric, and chemical properties of the MUT. FEF sensors are best visualized as a parallel plate capacitor (PPC) in which the plates have been separated and placed adjacently in the same plane. A unidirectional varying potential is applied to one plate electrode generating an exponentially decaying electric field perpendicular to the plane of the sensor. The generated field lines penetrate the MUT adjacent to the sensor and terminate on the opposite plate electrode inducing a current and voltage related to the attenuation of the electric field in the presence of the MUT. From these measurements of the dielectric response of the material, the various properties of the material can be obtained.

FEF sensors have been utilized in many applications and industries including the measurement of material properties in manufacturing [1], monitoring industrial processes [2], the measurement of coating thickness on aircraft [3], detection of degradation in power cables [4, 5], and measurement of physical and chemical changes in dielectrics [6, 7]. FEF sensors are practical in a wide variety of applications and have become more common due to their economical cost and versatility. Their use in dielectric spectroscopy has been well developed and is an accepted method of measuring the dielectric properties of a material. The results of this thesis specifically discuss

the design and implementation of FEF sensors to detect property changes in BMI composites, however many of the principles discussed generally apply to FEF sensors in any application.

1.2 Advantages and Disadvantages of FEF Sensors

FEF sensors are versatile non-destructive sensing devices that have found use in humidity detection, process control, quality control in manufacturing, and even as a control feature in consumer cellular devices. Their relatively low cost and the ability to tailor the sensor geometry for a specific function make them a practical choice for a variety of capacitive sensing applications. In some cases, accurate measurements may require sophisticated processing algorithms, or enhanced shielding, however, FEF sensors generally have very few drawbacks. The following discussion elaborates on the advantages and disadvantages of FEF sensors in detecting incipient thermal damage in composites.

1.2.1 Advantages of FEF Sensors in Detecting Damage in Composites

1.2.1.1 Single Sided Measurement

In comparison to other non-destructive testing methods, FEF sensors only require single-sided access to a material. Additionally, measurements do not require physical contact with the MUT allowing for rapid scanning of large surface areas. This is of benefit for the development of a field instrument where measurements can be conducted quickly to reduce aircraft service downtime due to inspection.

1.2.1.2 Material Penetration

Fringing electric fields penetrate through non-conducting materials, which is useful for measuring surfaces with external coatings or paint. This property is of particular benefit in aviation where aircraft are typically coated or painted to protect the body of the aircraft from oxidation, exposure to weather, and sun damage. Other NDE methods such as FTIR, require the removal of aircraft coatings prior to measurement which increases cost and evaluation time.

1.2.1.3 Economical

FEF sensors can be inexpensive depending on the accuracy and resolution required and are easily customized for an individual application. Supporting instrumentation electronics can be inexpensive, and measurements can be logged using common data capture testing hardware and software. In most cases, characterization of a material can be achieved with simple calibration and does not require advanced methods of analysis.

1.2.2 Disadvantages of FEF Sensors in Detecting Damage in Composites

1.2.2.1 Data Processing

In most cases, measurements only require simple calibration and detection of specific properties can be correlated to measurements of a sample with known physical or chemical properties. Yet some applications require sophisticated algorithms and additional data post-processing to achieve accurate results. In these cases, post-processing analysis can require extensive knowledge of the material to be tested and considerable data manipulation to produce the desired measurement results.

1.2.2.2 Noise Interference

Noise can significantly impact the measurement capability of FEF sensors depending on the excitation and measurement frequency required. Conductive materials around the sensor head can also impact the electric field lines and disturb measurements. Additional shielding, signal filtering, and data post-processing can reduce or resolve these issues, however, these enhancements must be balanced with increased cost and instrument complexity.

1.2.2.3 Sensor Measurement Limitations

FEF sensors utilize actuated electric fields thus measurements are limited to non-conductive or partially conductive materials. Additionally, the accuracy of measurements decreases as the distance from the plane of the sensor increases and effective measurement is generally limited to a few millimeters from the sensor head.

1.3 Scientific and Engineering Challenges

The work detailed in this thesis has several scientific and engineering challenges which are broadly categorized and described here.

1.3.1 Sensor Design

FEF sensor designs are challenging due to their susceptibility to external electric fields and noise and the difficulty in quantifying and visualizing induced electric fields. Sensor response is strongly affected by metal within close proximity of the sensor head due to interactions with the varying fringing electric fields and by external sources of noise which introduce significant error in measurements, as measured sensor values are extremely small. These sources of measurement error require additional shielding or changes in the sensor geometry to improve sensor signal to noise ratio. FEF sensors are constructed with a wide variety of electrode geometries and are typically configured for best performance in the desired application. Analytical modeling can be used to simulate simple sensor geometries, however, increased sensor complexity such as multi-channel sensors or exotic electrode configurations are too complex to solve for analytically. For these reasons, FEF sensor design is typically accomplished via parametric modeling and finite element simulations and sensor design can often be iterative.

1.3.2 Instrument Miniaturization

Sensor measurements require extremely sensitive electronics capable of a flat response across a broad frequency range, in consequence, the supporting instrumentation electronics include substantial circuitry for frequency compensation and signal conditioning. Dielectric spectroscopy is dependent on the frequency response of the material tested which is a limiting factor for analog electronics, particularly in current measurement, where frequency response of transimpedance amplifiers is limited without considerable frequency compensation circuitry. Similarly, as discussed in section 1.3.1, external noise introduces error in measurements and necessitates active filtering and additional shielding resulting in an increase in instrumentation size and cost. Thus, optimization of the instrumentation electronics is achieved through frequency response circuit simulations and interference testing to achieve ideal results.

1.3.3 Signal Processing

FEF sensor signal processing poses a significant challenge due to their susceptibility to noise, non-linear response, and the difficulty in equating measurements to material properties. In many cases, accurate measurements only require simple calibration, however, in some cases extensive data processing is required to interpret sensor response. Isolation of the measured physical, chemical, and structural properties of a material requires an understanding of the MUT and comprehensive frequency response analysis. Additionally, measured sensor values are minute and as a result identifying minor differences among similar materials requires highlighting the sensor response of individual measurements. Thus, measurement evaluation is achieved by accentuating sensor data via calibrated measurement normalization, derivative and differential processing, and multi-variate analysis.

1.4 Scope of Thesis

Figure 1.1 is a visual representation of the scope of work. This thesis details the theory, design, and implementation of FEF sensors to detect incipient thermal damage in BMI composites and investigates the feasibility of developing an instrument for NDE of thermally damaged composite aircraft. In addition, the thesis aims to better understand FEF sensor measurements of thermally damaged composites and identify technical considerations for future development of the technology.

Sensor Theory and Design: With respect to theory and design, this thesis attempts to develop an effective electrode geometry to evaluate BMI composites and discusses the general guidelines behind interdigital FEF sensor design. The configuration of sensor electrodes considerably impacts measurements and as such two FEF sensor geometries are discussed and the benefits and drawbacks of each are detailed.

Implementation: FEF sensor geometry and the supporting data processing methods are dependent on the material being measured and the detected properties of interest. The thesis attempts to develop processing algorithms to identify thermal exposure in BMI composites and discusses the design challenges and sensor enhancements implemented to improve sensor accuracy.

Instrument Development: The ability to evaluate composite aircraft in the field is critical to their safety and operation and is central to the investigation presented in the thesis. Thus, the feasibility

of constructing a portable instrument for practical application is investigated and the required supporting electronics and associated design challenges are discussed.

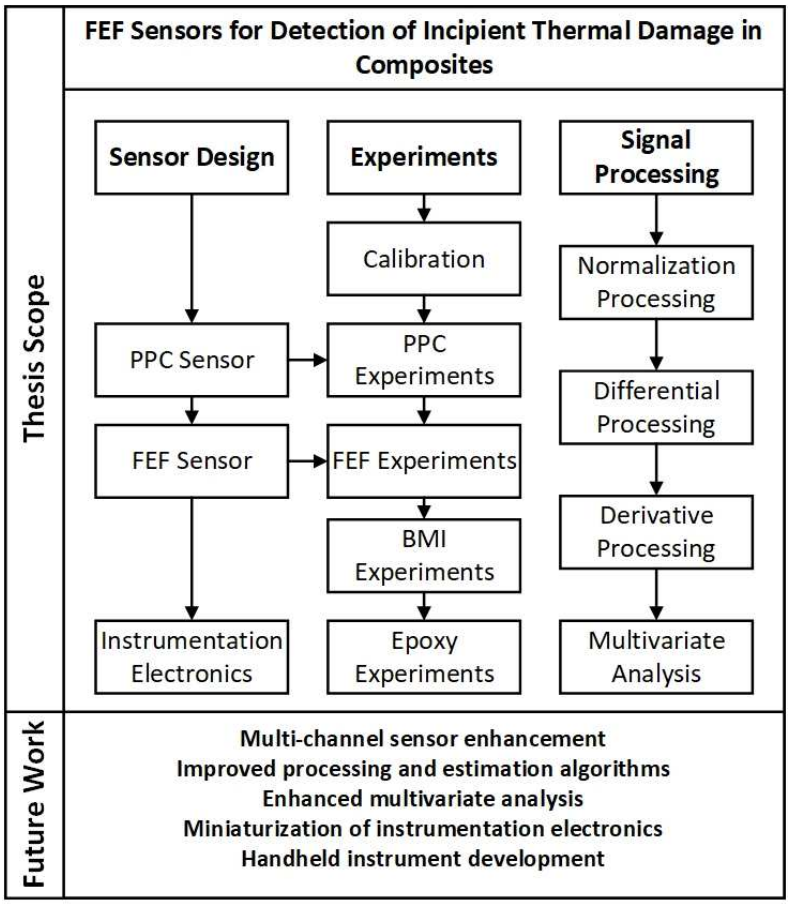

Figure 1.1. Scope of thesis and future work.

1.5 Contributions of the Thesis

There are three significant contributions of this thesis to science and engineering. First, this thesis demonstrates the capability of FEF sensors to detect and quantify non-visible thermal damage in composites. Dielectric analysis has been performed on other composites utilizing standard dielectric spectroscopy test equipment but has not been implemented with FEF sensors. Confirming the effectiveness of FEF sensors in detecting incipient thermal damage in composites builds on previous applications of these sensors and expands their use in dielectric NDE scenarios.

Second, the data processing algorithms and characterization techniques developed in this thesis are applicable to the development of future uses of FEF sensors in composite evaluation. Enhanced versions of the algorithms presented are useful for developing instrumentation for in-

situ measurements and support the development of impedance tomography imaging in composite evaluation use. Additionally, these processing techniques act as a foundation for the characterization of similar composite materials used in other structural applications such as automotive and naval industries.

Finally, the miniaturization of FEF sensor instrumentation supports the development of a portable instrument for non-destructive evaluation of thermally damaged composite aircraft. In addition to composite evaluation and algorithm development, this thesis acts as a proof of concept and provides a foothold for further investigation in the development of a portable non-destructive instrument for use practical evaluation of composite materials. Such an instrument enhances existing methods to non-destructively detect damage in composites in commercial and military aircraft applications and would be easily adapted for use with naval and automotive composite materials.

Chapter 2. Background and State of the Art

2.1 FEF Sensors Background and State of the Art

2.1.1 Basic Operation of Fringing Electric Field Sensors

2.1.1.1 Fundamentals of Fringing Electric Field Sensors

FEF sensors function in much the same way as conventional capacitors, an example of which is the parallel plate capacitor (PPC), whereby a dielectric material is inserted between the plate electrodes to enhance the performance and electrical properties of the capacitor by exploiting the relationship between capacitance and the dielectric properties of the material used. The dependence of the properties of the capacitor on the dielectric material used allows for the characterization of the material by measuring the current, voltage, and capacitance of the capacitor. Thus, in the case of a PPC, an applied voltage across the plate electrodes generates linear field lines through the material and its measured transconductance and transcapacitance are linearly related to the permittivity and conductivity of the material.

In many cases one-sided dielectric measurements are required for practical application, prohibiting use of the “pitch and catch” geometry of the PPC. Figure 2.1 shows how a single-sided

FEF sensor can be created from a PPC by placing the electrodes of the conventional PPC geometry in the same plane adjacent to one another. Much like the PPC, FEF sensor operation utilizes a unidirectional varying potential which is applied to one electrode thus generating an exponentially decaying fringing electric field perpendicular to the plane of the sensor. The generated field lines penetrate the MUT adjacent to the sensor and the attenuation of the electric field is measured and correlated with the dielectric response of the material, from which physical properties of the material can be obtained. Unlike PPC geometries, FEF sensor geometries have a non-linear response and cannot be solved analytically, as such the sensor response to material properties is typically characterized experimentally.

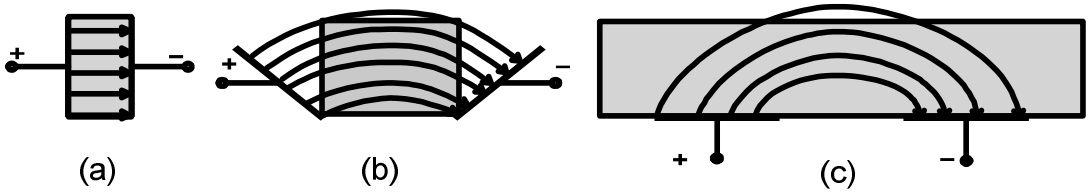

Figure 2.1. The transition of electrodes from a parallel plate capacitor (a) to a FEF sensor. (c).

Penetration depth of the fringing electric field is a notable limiting element of FEF sensors and is dependent on the geometry of the electrodes and the magnitude of the applied potential. The primary metric for penetration depth is the spatial wavelength, which is defined as the distance between two adjacent sensing or driving electrodes. The effective field depth is generally defined as one-third of the spatial wavelength [8]. Measurement of multiple depths is possible with the use of a multi-channel sensor consisting of multiple sets of electrodes with different spatial wavelengths [9]. Figure 2.2 shows how a multi-channel FEF sensor with multiple spatial wavelengths measures at multiple depths in a material. Multi-channel sensors provide more comprehensive information about the spatial distribution of properties in the material and improve sensor resolution.

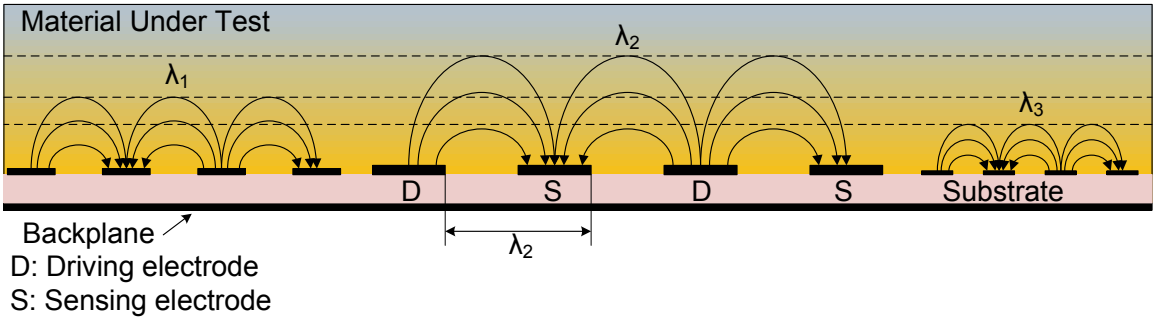

Figure 2.2. An example of a FEF sensor with multiple spatial wavelengths.

2.1.1.2 Fundamentals of Dielectric Spectroscopy

Dielectric spectroscopy is a well-established method to measure the properties of dielectric materials that relies on the response of the material to an external electric or magnetic field. Naturally polar molecules or induced dipoles within the material rotate to align opposite with the applied field. When the applied field is removed the dipoles return to their original amorphous state within the material. This response is called relaxation and in most cases is unique to a material across a frequency range and is generally quantified in terms of its dielectric permittivity. The complex dielectric permittivity $\varepsilon^*(\omega)$ is represented as:

$$\varepsilon^*(\omega) = \varepsilon'(\omega) - j\varepsilon''(\omega) \tag{2.1}$$

where $\varepsilon'(\omega)$ and $\varepsilon''(\omega)$ represent the real and imaginary components of the permittivity respectively. The real contribution to the permittivity is primarily due to its capacitive energy storage of the material while the imaginary part is due to energy loss. Loss is a function of frequency thus, the contribution of the excitation response of a material can be identified across a broad frequency range. Figure 2.3 shows the relative contribution of the physical properties of a dielectric to the relaxation response across the dielectric spectrum.

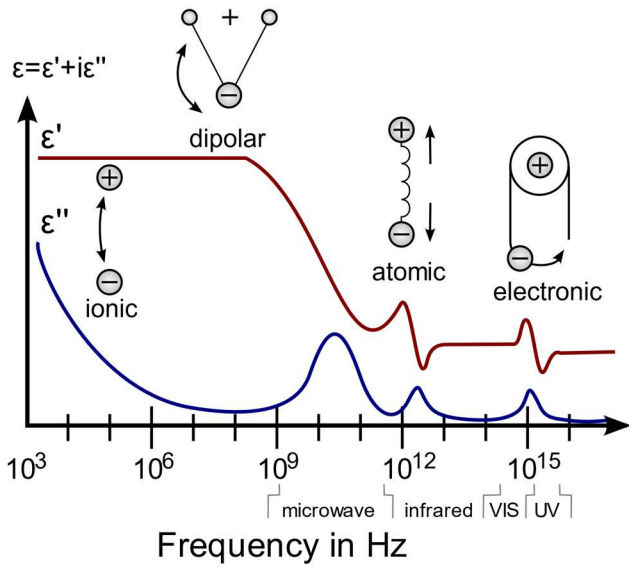

Figure 2.3. The dielectric response spectrum with respect to the real and imaginary parts of the permittivity.

Dielectric spectroscopy requires an electrochemical or dielectric analyzer consisting of a signal generator and current and voltage analyzers connected to opposing electrodes. The material of interest is inserted between the two electrodes and a signal, typically a sinusoidal potential, is applied to one electrode while the voltage and current are measured from the opposite electrode. Using this method, and with an understanding of the geometry of the electrodes, it is possible to measure the capacitance from which the dielectric permittivity, dielectric loss, and other properties of the MUT can be determined. In the case of a PPC the capacitance is given as,

$$C(\omega) = \frac{\varepsilon^*(\omega)A}{d} \tag{2.2}$$

where $C(\omega)$ is the frequency dependent capacitance, A is the cross sectional area of the electrodes and d is the distance between the electrodes. The permittivity can be calculated from the measured current and voltage with the relationship:

$$I = j\omega CV \tag{2.3}$$

where I is the current induced on the sense electrode and V is the sinusoidal voltage applied to the drive electrode. Combining (2.2) and (2.3) results in

$$\varepsilon^*(\omega) = \frac{Id}{j\omega VA} \tag{2.4}$$

Utilizing wideband spectroscopy and performing this analysis across a wide frequency range allows for the identification of individual properties of a material dependent on the measured frequency response [10].

2.1.2 State of the Art in FEF Sensing

Capacitive sensors such as FEF sensors have been utilized in numerous applications, the most common of which has been in humidity detection and moisture concentration. Their ability to measure material properties has seen use in many applications and industries including the measurement of material properties in manufacturing [1], monitoring industrial processes [2], the measurement of coating thickness on aircraft [3], detection of degradation in power cables [4, 5], measure physical and chemical changes in dielectrics [6, 7].

Modern developments in FEF sensing technology can be broken into three general categories of sensors based on their application. The categories described below do not comprehensively encompass all applications of fringing electric field sensors, however, they do describe the majority of use cases. The categories are as follows:

i) capacitive sensors for position measurement, proximity control, and similar applications [11-13];
ii) single and multi-wavelength sensing for the detection of chemicals, gasses, or humidity [14-16];
iii) single and multi-wavelength sensing for spectroscopic impedance, dielectric or physical phenomena [17-21]
iv) electrical impedance tomography sensor arrays for industrial and biomedical 3D imaging [22-25].

Much of the current research related to the development of FEF sensors is focused on the optimization of sensor geometry for specific applications. Applications include: electrochemical

sensing for pharmaceutical applications, impedance spectroscopy for biological and food characterization and analysis, and in similar fashion to this thesis, for the non-destructive evaluation of a variety of materials.

2.2 Introduction to Composite Evaluation

Aircraft require regular inspection and, in some cases repair, to maintain their safety and performance throughout their lifespan. This includes evaluating the stresses and strains incurred on the aircraft and monitoring the strength of materials that make up its body and structure. Incomplete identification and repair of damage results in a weakening of the aircraft and subsequently increases the risk of mechanical faults or structural failure. To mitigate this risk and assist in preemptively repairing damage, several NDE methods have been developed to evaluate aircraft which are capable of detecting fatigue and damage without the need to remove material from the aircraft under test. These methods vary with regard to the section of the aircraft under inspection, the material being evaluated, and the type of damage to be measured [26].

Recent developments in the structural performance of composites and a reduction in their manufacturing cost has seen an increase in their use in commercial and military aircraft due to their lighter weight and greater strength in comparison to metals. Unlike metals, composites are primarily composed of organic materials and require advanced methods of analysis due to their layers, internal structure, and chemical properties. Heat sources such as lightning strikes, engine emissions, and battery fires can cause thermal damage in composites in the form of additional cure reactions, physical aging, and chemical aging, all of which influence the mechanical properties and toughness of the material [27-30]. Thermal damage causes changes in the composite polymorphic matrix which weakens the material without producing physical or visible damage making it undetectable using conventional NDE techniques.

The most common NDE methods used to evaluate both metal and composite aircraft include Ultrasonic Testing (UT), Radiography, and simple visual inspection. Methods such as UT and XCT are widely accepted in the detection of physical damage such as cracking, voids, delamination, and micro-cracking in composites. Although physical damage in composites can be detected via these techniques, at the time of this writing there is no non-destructive testing method to detect thermal damage prior to physical degradation of the material. C-Scan UT is currently used to evaluate composites post-cure, however, it is limited to the detection of physical damage

and may not detect thermal damage until the material experiences matrix cracking, fiber fracture, or fiber debonding and loses as much as half of its mechanical strength. Thus, existing methods to detect and evaluate damage in metal aircraft are not capable of comprehensively evaluating composite aircraft.

2.3 Composite NDE Methods and State of the Art

2.3.1 Visual Inspection

Visual inspection benefits from its inherent simplicity and requires little more than a trained individual and a microscope. Visual inspections are performed quickly and can be used to identify cracks and stress damage in composites, however, inspections are limited to surface defects. As such, this method is primarily used to identify the need for more detailed inspection using other NDE methods capable of detecting internal damage or non-visible weakening of the material.

2.3.2 Radiographic Methods

Radiography methods span a wide variety of techniques such as x-ray computed tomography (XCT) and gamma-ray radiography which detect different forms of damage. XCT is used to image the interior features of an aircraft in three dimensions while gamma-ray radiography is useful for detecting delamination and voids in composites. Radiographic methods present several disadvantages including requiring access to both sides of the surface being inspected, difficulty detecting damage perpendicular to the emitted energy beam, and an inherent radiation risk during measurement [26].

2.3.3 Ultrasonic Testing

There are multiple forms of UT which vary in transmission and sensing technique and detection of damage is dependent on wave propagation velocity and amplitude in the MUT. UT allows for rapid scanning and can accurately detect cracks both in size and location as well as their relative orientation. This method requires a skilled operator and a test sample for accuracy and is most useful in an assembly line or production environment where a single part or design must be tested repeatedly. UT is the primary method of NDE in aerospace composites and is used to detect voids and lamination defects which may occur in manufacturing during the cure process [26, 31].

2.3.4 Infrared Thermography

Also referred to as infrared thermal wave imaging, Infrared thermography (IRT) is an NDE method that utilizes thermal excitation and infrared image processing to detect damage or defects in a wide variety of materials. Initially developed in the 1980s the technology has seen rapid advancement in recent years as the demand for non-destructive testing has grown and encompasses a variety of heating, imaging, and processing methods that target damage in particular materials. Current implementations of the technique are capable of measuring damage in metallic and non-metallic materials, coating thicknesses, structural characteristics and the depth of damage in a material and scanning of materials is rapid and can cover large surfaces. However, thermal measurements can be depth limited to a few millimeters and may require a variety of bulky instruments depending on the material and damage of interest [32, 33].

2.3.5 Fourier-transform Infrared Spectroscopy

Fourier-transform infrared (FTIR) spectroscopy sensing is a more recent development of in-situ NDE techniques that presents the possibility of detecting incipient thermal damage in composites. FTIR is a widely used method for chemical characterization of materials and can analyze chemical changes in composites. Although this technique has been used to correlate incipient thermal damage to a reduction in strength of epoxy-based composites and BMI CFRP, accurate measurements are dependent on the surface finish and can be affected by fiber orientation in the composite. FTIR measurements are also limited by depth, with internal measurements requiring the removal of material during repair to detect incipient thermal damage at depth [34-37].

2.4 Chapter Summary

Electric field sensors operate in much the same way as a PPC whereby the performance of the capacitor is dependent on the dielectric material placed between its electrodes. In the case of FEF sensors, the electrodes of the sensor reside in the same plane generating fringing field lines and allowing for single-sided measurements. Additionally, FEF sensors can be enhanced with multiple channels which act to increase the spatial resolution of the sensor, allowing for detection

at multiple defined depths in the material. Although FEF sensors often only require simple calibration, some measurements necessitate extensive data processing and analysis for effective use.

Measuring the dielectric properties across a frequency range is a common method used to characterize materials known as dielectric spectroscopy. By measuring the response of a material across a broad frequency range, the physical, chemical, and geometric properties of the material can be isolated. The transconductance, transcapacitance, and complex dielectric permittivity for a material can be obtained from these measurements and used to quantify its physical properties and identify the material in question.

FEF sensors have been used in a wide range of applications from industrial process control to consumer proximity sensing. Modern developments in FEF sensors can be categorized as general capacitive and proximity sensing, material measurement and evaluation, and impedance imaging. These developments are primarily focused on the evolution of the coplanar sensor with enhancements to geometry and its use in new applications such as biological detection, food characterization, and material evaluation. The ability of FEF sensors to rapidly evaluate the physical and chemical properties of a material make them an excellent solution for detecting thermal damage in composite aircraft.

Aircraft require regular structural inspection to evaluate the stresses and strains incurred during service to maintain their safety and performance. The increased adoption of composites in aviation has generated demand for more comprehensive methods to evaluate these materials as existing NDE methods used to evaluate metal aircraft are not capable of detecting non-visible thermal damage in composites. While common NDE methods such as visual inspection, XCT, and UT are effective at detecting cracks, voids, delamination, and other forms of physical damage, they are not capable of detecting insipient thermal damage in the form of chemical changes or cure processes in composites. FTIR has the potential to detect such damage, however, measurements are primarily limited to damage near the surface of the material and exterior coatings must be removed from the aircraft prior to evaluation.

Chapter 3. Damage Detection Methodology

3.1 Sensor Topology

3.1.1 Parallel Plate Sensor

Two electric field sensors were purpose built to evaluate the thermally damaged square composite samples obtained for testing. The primary sensor design utilized a conventional PPC geometry or a "pitch and catch" configuration whereby a drive signal is generated on one electrode and a signal is induced on an opposing electrode. The addition of a guard surrounding the sense electrode, which maintains the same potential as the sense electrode, and a grounded backplane behind the sensor, provide shielding and reduce the fringing of the field lines within the sensor. Much like a conventional PPC, this geometry creates perpendicular field lines between the electrodes, providing a linear sensor response. The MUT is placed between the electrodes and completely covers the active sensing surface. Because of its similarities to a PPC, the transcapacitance and transconductance are linearly related to the conductivity and permittivity of the MUT and knowledge of the sensor area and distance between the drive and sense electrodes allows the material properties to be obtained.

With these principles in mind, the parallel plate capacitor (PPC) sensor was cut from two-sided copper-clad FR4 and utilizes a 2.5 cm x 2.5 cm sensor surrounded by a 2.5 cm thick square guard with a small 0.5 mm gap etched between the guard and the sense electrode. The sense electrode is connected to the core of the "sense" coaxial cable while the shield is connected to the backplate and guard. To allow for sample insertion without contacting the drive plate, the distance between the drive and sense electrodes was fixed at 7mm using nylon screws. Figure 3.1 shows an isometric view and a side view of the PPC sensor.

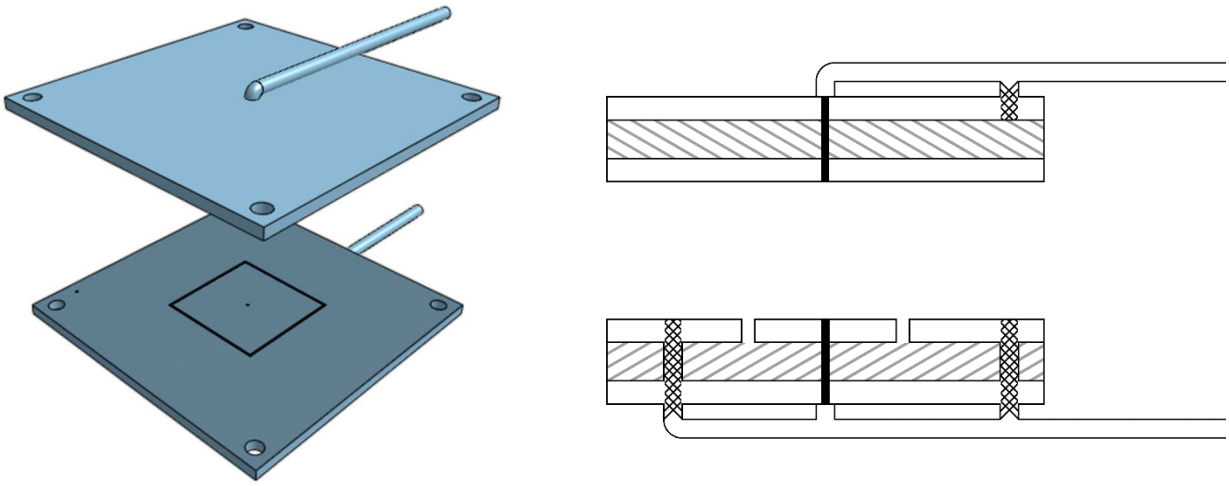

(a) *(b)*

Figure 3.1. *The parallel plate capacitor sensor configuration in 3D (a) and side through (b) views.*

3.1.2 Fringing Electric Field Sensor

To accommodate the development of a practical instrument, a one-sided FEF sensor was also designed to characterize the response of thermally damaged samples. As mentioned previously, FEF sensors are best visualized as a parallel plate capacitor with opposing coplanar plates. The field lines generated by the drive electrode penetrate the material adjacent to the sensor and terminate on the sense electrode, however, unlike the PPC sensor the FEF sensor electric field is non-linear and typically has a smaller signal strength concentrated close to the electrodes. The characteristics of a FEF sensor are dependent on the shape, size, and orientation of the electrodes and define the field strength and resolution of the sensor while the distance between the electrodes allows for a defined field penetration depth.

The FEF sensor discussed here utilizes interdigital electrodes, which can be thought of as two sets of interlocked fingers, to increase local electric field strength and was developed using the design principles explained in [8, 9]. It is a single channel sensor with a functional surface area of 3 cm x 3 cm, limited by the minimum size of the composite samples to be tested. The spectral wavelength of the sensor, defined as the distance between two adjacent electrode fingers of the same type, is 1.2 cm and the related penetration depth is approximately 3.6 mm. The sensor was

etched on one side of copper-clad FR4 circuit board with the opposite side left unetched. Shielded coaxial cables were attached via two pads, one on either side of the sensor to create drive and sense electrodes, and the unetched backplane is connected to ground to provide electromagnetic shielding. Figure 3.2 shows the layout drawing of the sensor plate.

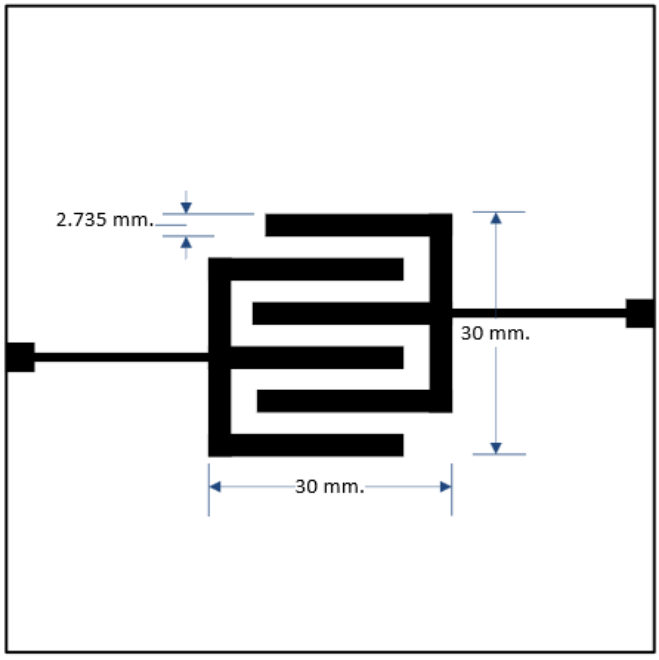

Figure 3.2. *The electrode layout for the FEF sensor, in this configuration the electrodes are reversible. The guard layer is on the opposite side of the sensor and is not visible in this image.*

To account for the increased noise sensitivity of the FEF sensor, shielding was developed in the form of a clamshell Faraday cage. The clamshell shield was designed in CAD to interface directly with the backplane of the FEF sensor and was covered in conductive copper tape following 3D printing. Figure 3.3 shows the rendered 3D model of the shield without the FEF sensor. The shield assembly accepts sensors of up to 7.5 cm x 7.5 cm in size and allows for the position of the sensor to be fixed relative to the shield. Figure 3.4 shows tests using this shielded configuration significantly reduced variance in comparison to previous measurements and reduced offset noise in measurements by nearly a factor of four.

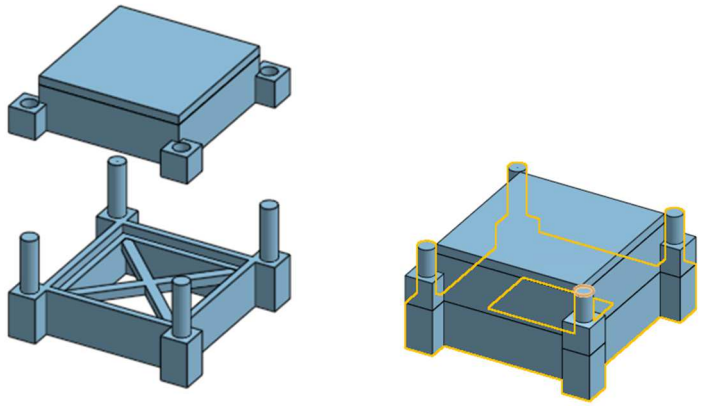

Figure 3.3. *The 3D printed shield assembly for the FEF sensor.*

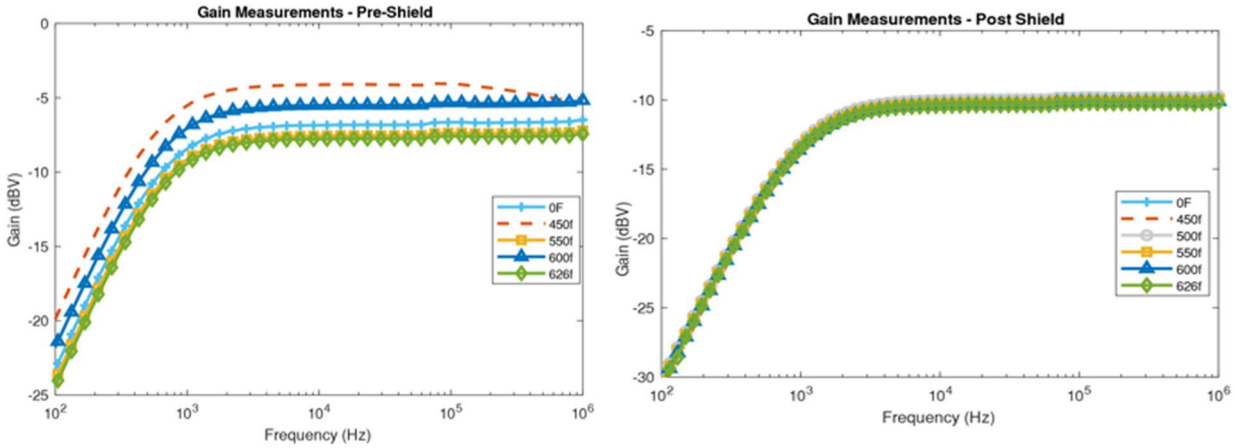

(a) **(b)**

Figure 3.4. *The fully shielded assembly allowed for a significant reduction of noise throughout each test.*

3.2 Instrumentation

3.2.1 Illionix Dielectric Spectroscopy Meter

Two instruments were utilized to obtain dielectric data for composite identification and analysis, an Illionix Dielectric Spectroscopy Meter (DSM) and a Solartron 1260A Gain Phase Analyzer. Initial dielectric measurements were achieved utilizing the Illionix DSM, which was selected due to its small size, compatibility with existing NDE and general testing equipment, and

versatility in configuration. The DSM, shown in Figure 3.5, is capable of measuring the capacitance and complex permittivity from sub 1 Hz to 100 kHz with a peak generator voltage of 10 V. Additionally, the instrument supports multi-wavelength sensor topologies via three independent SMA connections and provides data acquisition and processing via LabVIEW software and a National Instruments interface card.

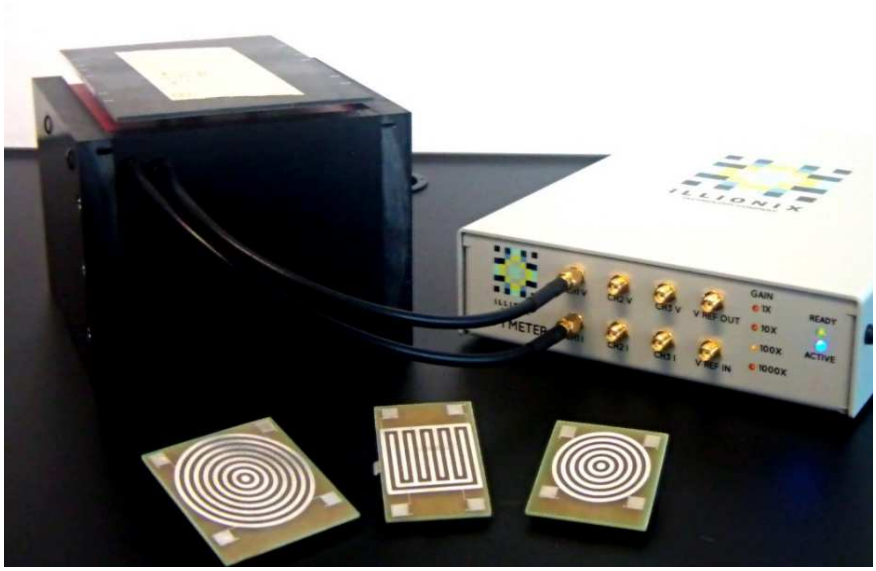

Figure 3.5. *Illionix Dielectric Spectroscopy Meter and application-specific FEF sensors.*

Although the Illionix DSM provides a variety of configuration options and comprehensive dielectric measurement data, its peak measurement frequency is a limitation in measuring BMI composites. Prior investigations into the dielectric properties of similar BMI composites indicated increased relaxation response at frequencies exceeding 100 kHz. Measurements utilizing the DSM indicated that the internal sensing amplifiers were frequency limited and overdriven above 70 kHz, prompting the procurement of an instrument with a broader frequency range.

3.2.2 Solartron 1260A Gain Phase Analyzer

The Solartron 1260A Gain Phase Analyzer was the primary instrument used to interface with and collect data from the PPC and FEF sensors. The instrument benefits from a significantly broader frequency range in comparison to the Illionix DSM allowing for measurements up to and exceeding 1 MHz, however unlike the DSM it is not capable of directly measuring capacitance and permittivity without additional equipment and only supports two measurement channels in its

standard configuration. Furthermore, the instrument is intended for a laboratory environment and is too large and unwieldy to be used for NDE field measurements. Figure 3.6 shows a typical measurement configuration utilized with either instrument, in this case, the Solartron 1260A is configured with a FEF sensor.

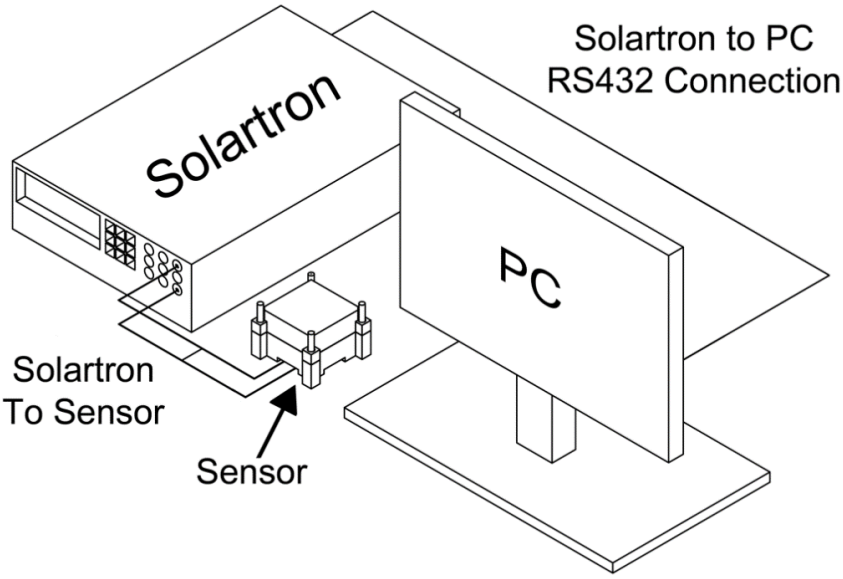

Figure 3.6. *The Solartron 1260A test setup configuration.*

Initial testing with the Solartron 1260A was achieved using BNC to alligator clip cables that arrived with the instrument, however, these cables did not allow for a fully shielded test setup and proved to be difficult to configure without introducing measurement error due to noise and poor electrical contact. Additionally, due to the inherent capacitive inefficiency of both sensor designs, the limited current generated on the sensor electrode prevented the instrument from accurately measuring the sensor response without additional modifications. A fully shielded cable configuration was developed to remove these sources of error utilizing shielded BNC to SMA connectors and shielded capacitance of 5 pF added in parallel with the sensor to provide additional current while maintaining the signal to noise ratio. This shielded test configuration yielded a decrease in offset measurement noise of up to 32%, allowing for a more accurate measurement of the features of interest of the composites. Figure 3.7 shows a comparison of the initial and improved Solartron configurations.

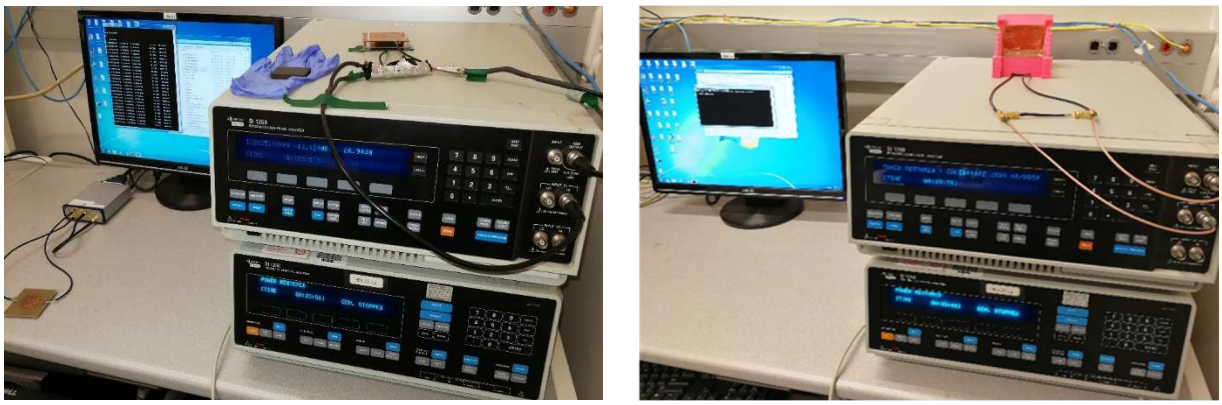

(a) **(b)**

Figure 3.7. *The previous configuration (a) utilizing alligator clips and the improved configuration (b) with fully shielded BNC to SMA cables.*

3.3 Signal Processing

Observation and analysis of test measurements resulted in a data processing algorithm that normalized measured data in gain (dB) against the frequency (Hz) of the measurement. This was accomplished using PPC data by first dividing each dataset by the thickness of the associated sample to remove sample thickness as a variable. The data is then pinned at a frequency of interest where the magnitude of each measurement is nearly equal. This data point is chosen by the user, thus making our algorithm a human-assisted process. The data is then normalized to a known undamaged sample measurement that was typically labeled as the "No Heat" or "0 °F" test set and plotted. Variation in the sample gain measurements is accentuated via pinning and highlights sample response relative to frequency.

3.3.1 Representative Function for a Test Set on a Single Sample

For any test set on a single sample with voltage responses as a function of frequency, $\{V_1(f), \ldots, V_n(f)\}$, we must define a process of getting an aggregate $V_x(f)$ from the set which is representative of the sample. The simplest way to define $V_x(f)$ is the average,

$$V_x(f) = \frac{\sum_{i=1}^{n} V_i(f)}{n} \tag{3.5}$$

However, individual test runs may contain noise or test sets may be invalid and have a high variance. Integrating over each test, noisy test sets will yield significantly higher or lower values than reliable tests, so the tests with median integrations can be taken as reliable. Defining f_{start} and f_{stop} as the starting and stopping frequencies of the tests, the set of integrations is defined as $U:\{V_1, \ldots, V_n\}$, where

$$V_i = \int_{f_{start}}^{f_{stop}} V_i(f)\,df, \ \forall i \in 1,\ldots,n \tag{3.6}$$

The set of the three most reliable tests can now be defined as $\{V_a(f), V_b(f), V_c(f)\}$ with

$$V_a(f) = V_i(f) : argmin(V_i), \ V_i \in U \tag{3.7}$$

Removing $V_a(f)$ from U,

$$V_b(f) = V_i(f) : argmin(V_i), \ V_i \in U \tag{3.8}$$

Now, removing $V_b(f)$ from U,

$$V_c(f) = V_i(f) : argmin(V_i), \ V_i \in U \tag{3.9}$$

So, a reliable average that is more representative of the sample can be defined as

$$V_x(f) = \frac{V_a(f) + V_b(f) + V_c(f)}{3} \tag{3.10}$$

3.3.2 Dataset Normalization

Two forms of dataset normalization are utilized, the first is intended to remove error due to thickness variation of each sample when measured using the PPC sensor. This error is due to the contribution of the thickness of the material to the capacitance of the sensor. The associated data processing algorithm is represented as follows: Given a set of n samples with thicknesses $\{t1, \ldots, tn\}$ and representative voltage responses $U:\{V_{x1}(f),\ldots,V_{xn}(f)\}$, the set of thickness normalized voltage response $T:\ \{V_{t1}(f),\ldots,V_{tn}(f)\}$ can be found as

$$V_{ti}(f) = V_{xi}(f) \;/\; t_i \;\forall i \in 1,\ldots,n \tag{3.11}$$

The second form of normalization utilizes a chosen dataset as a calibration measurement and compares the relative magnitude of each measured sample to the known sample dataset at each frequency. This relationship is represented as follows: Let $V_{NH}(f)$ be the voltage response of the known no heat sample as a function of frequency, f. Let $U : \{V_{x1}(f),\ldots,V_{xn}(f)\}$ be the set of representative functions derived from test sets on individual samples. A normalized set can be defined as $\{V_{N1}(f), \ldots, V_{Nn}(f)\}$, where

$$V_{Ni}(f) = V_{xi}(f) - V_{NH}(f), \;\forall i \in 1,\ldots,n \tag{3.12}$$

3.3.3 Data Point Pinning

Pinning is useful when sample paths (functions) obtained from data appear to experience a similar phenomenon at a certain point. In the case of our data, when voltage responses appear to converge at a certain frequency but fail to converge completely. In this case, pinning can be used to artificially force all functions to converge at that point for the purpose of observing absolute change thereafter. Consider once again the set of representative voltage responses, $U : \{V_{x1}(f),\ldots,V_{xn}(f)\}$. Let f_o be the frequency at which pinning will be applied. Then the set of pinned voltage responses would be $\{V_{P1}(f),\ldots,V_{Pn}(f)\}$, where

$$V_{Pi}(f) = V_{xi}(f) - V_{xi}(f_o), \;\forall i \in 1,\ldots,n \tag{3.13}$$

3.3.4 Combined Algorithm

Multiple combinations of each processing method were utilized in identifying relevant properties within the data. The final algorithm applied these steps as follows: find representative function (either average all or average median of three), thickness normalization, known good sample normalization, and pinning. This algorithm, implemented in MATLAB, is modular can accommodate additions such as the implementation of auto-formatting of plots, and the selection of calibration dataset's for measurement comparison to simplify data processing.

3.4 Additional Effort Vectors

3.4.1 Illionix DSM Enhancement

The Illinoix DSM is an analog instrumentation to sensor interface which utilizes a National Instruments PCI-6154 card and LabView software to provide measurement control and calculate the dielectric response of the material in the sensor. The 100 kHz limitation of the device is primarily due to the analog interface and the frequency limitations of the components and compensation circuitry used in its construction. There were two primary goals of this project: first, to design a new version of the device such that the range of measurable frequencies is higher, and second, to explore the possibility of developing a hand-held version of the analyzer.

The instrument was disassembled to reverse engineer the circuitry and improve the frequency response with updated components. Figure 4.8 shows a deconstructed view of the instrument and its primary circuit board. A bill of materials and a schematic of a single channel of the instrument were developed from observation and circuit testing of the board. The resulting single channel schematic is shown in Figure 3.9.

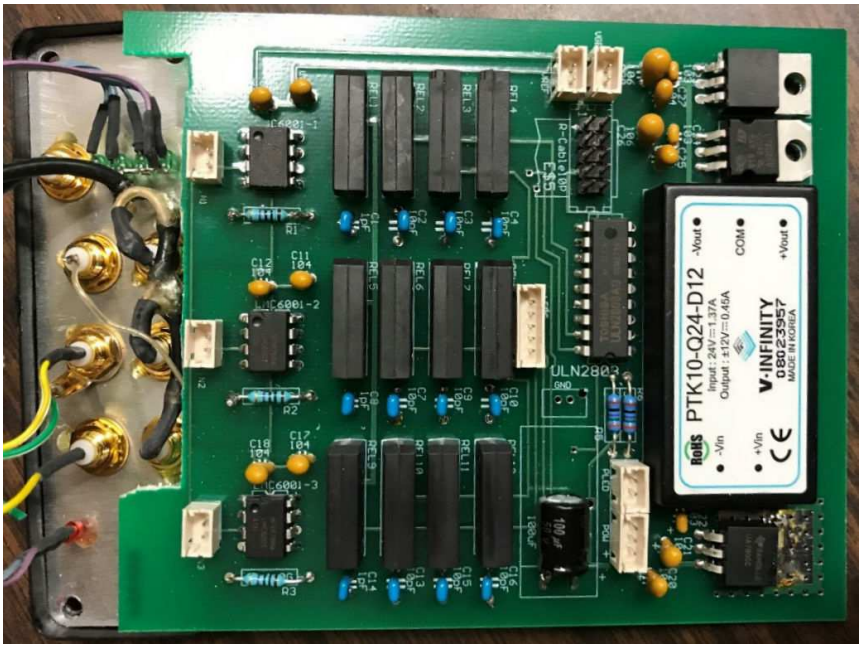

Figure 3.8. *Top down view inside of the Illinoix DSM with three input channels and SMA sensor interface bracket.*

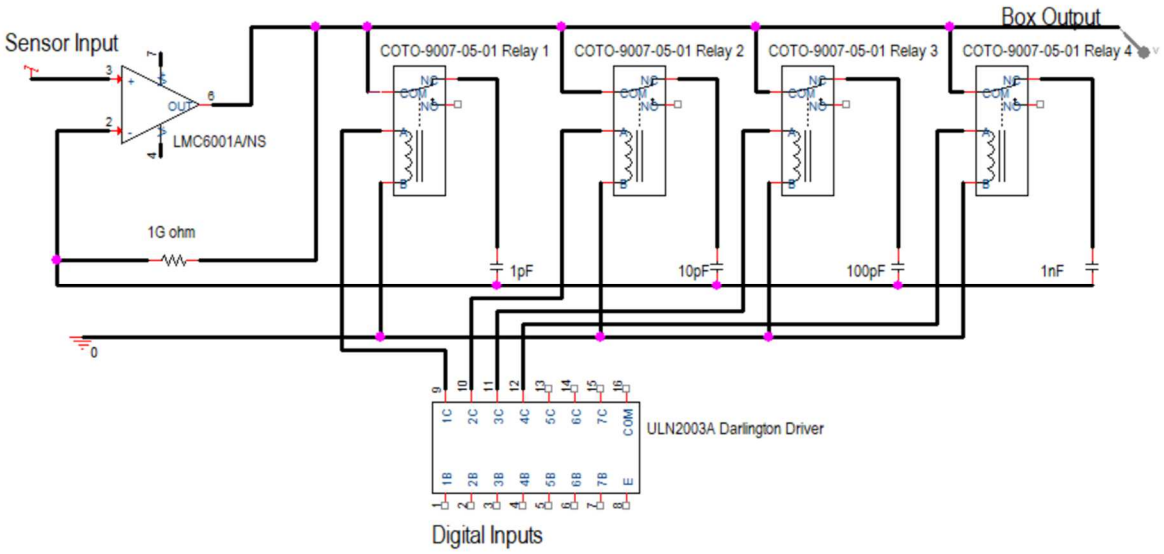

Figure 3.9. *Single-channel schematic of the Illinoix DSM showing the frequency compensated output.*

Utilizing these resources, a single channel prototype was constructed using updated components to simplify the design for characterization and performance testing. The ULN2003A

Darlington driver takes digital inputs from the LabVIEW software interface via the National Instruments PCI interface card and drives the individual relay circuit loops. Input to the single-channel circuit is the non-inverting input of the Op-Amp, which is the response signal from the sensor. The circuit output is returned to the National Instruments PCI interface as an analog signal.

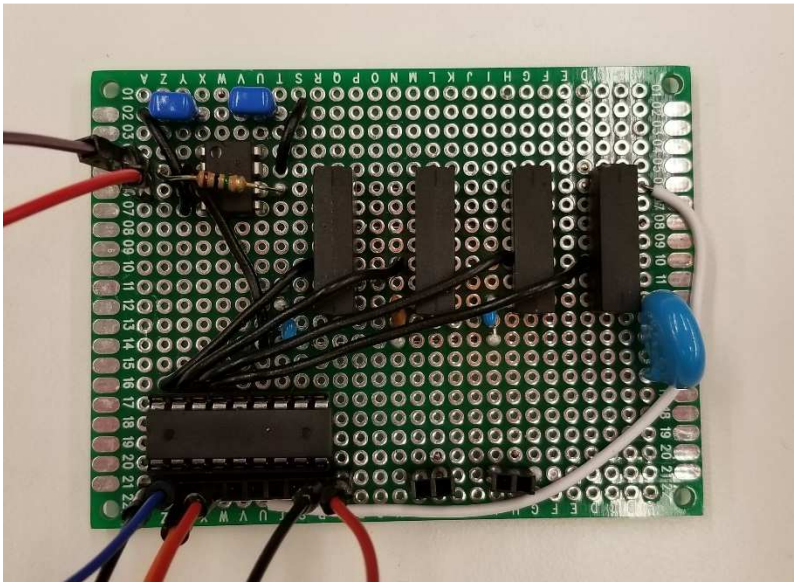

Figure 3.10. *A single channel prototype output circuit of the Illionix DSM. Digital control wires at the bottom of the image lead to a feedback controller and wires to the upper left of the image are the inputs from the sensor.*

Observations of the circuit indicate that: 1) the drive signal is generated directly by the LabVIEW software and the National Instruments interface card, 2) the relays are digitally driven from the interface card through the Darlington driver while the voltage and current output of the circuit are measured by the analog interface of the PCI card, 3) the device alters the frequency response of the transimpedance circuit by switching the relays open and closed to adjust the capacitive feedback. Future efforts in this project will require a circuit simulation in SPICE and characteristic testing of the circuit prototype with a signal generator.

3.4.2 Signal Generator Amplifier

Prior testing with the Illionix DSM instrument utilized a peak generator output signal of 10 V to produce results, however, the Solartron 1260 is limited to 3V RMS or approximately 4.2 V peak.

To improve the signal-to-noise ratio, increase induced current on the sensor, and possibly increase the relaxation response of the material, a signal amplifier was designed to increase our peak generator magnitude to a 10 V peak.

The initial design utilized an instrumentation amplifier, AD8432, that was previously obtained from Analog Devices as a sample. We created a simple board layout and configured the amplifier for a gain of two, however initial testing demonstrated a slew rate limitation of the amplifier above frequencies of 200 kHz. Using this knowledge and a better understanding of the circuit requirements we selected a replacement amplifier, the AD844, which is intended for high gain inverted amplification and transimpedance circuits but has a flat response at frequencies exceeding 10 MHz and is capable of driving capacitances in excess of 100 pF. The amplifier and its associated circuit board layout are shown in Figure 3.11.

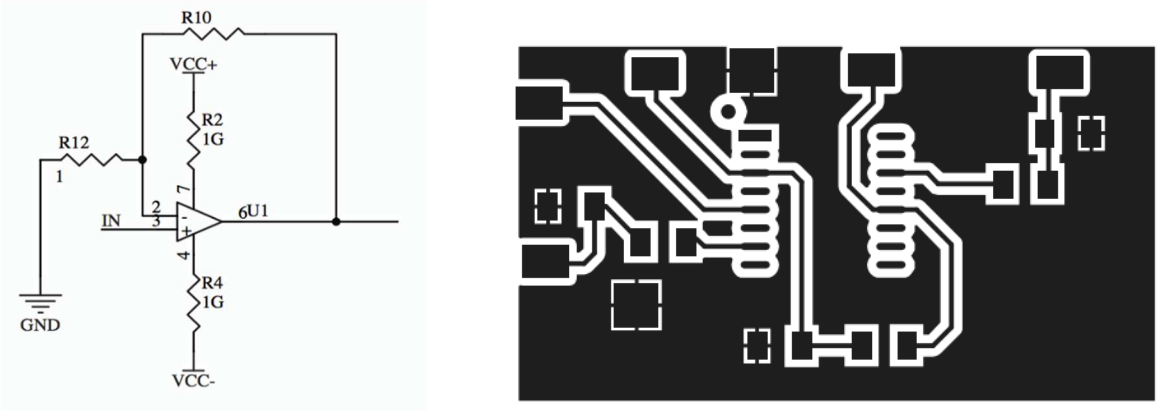

(a) *(b)*

Figure 3.11. *The AD844 generator amplifier circuit (a) and its associated board layout (b).*

The generator amplifier is configured using the AD844 in a simple non-inverting op-amp circuit topology. The non-inverting input of the AD844 is limited to 1 V peak signals thus the generator signal input must be limited to 0.707 V RMS, however, this would allow for more than 10 V peak-to-peak generator signal magnitude. Thus, the amplifier gain is set to 11 by the non-inverting feedback resistor network, and an RC network with decoupling capacitors is placed on each rail to reduce supply noise.

3.4.3 Transimpedance Amplifier

Measurements achieved with the Solartron 1260 instrument provided only gain and phase response of the sensor. Obtaining measured capacitance via a transimpedance amplifier (TIA) would allow the calculation of tan-delta and more comprehensive dielectric analysis. Efforts to create a TIA circuit to obtain estimated sample capacitance followed two vectors. The first involved utilizing the same instrumentation amplifier from the generator amplifier circuit and simply connecting the sensor to one of the gain resistor inputs of the amplifier while grounding all other reference pins. The second vector was to utilize a high bandwidth TIA or a TIA with a feedback ladder that would compensate for frequency response as characterized in [38].

Utilizing an AD8432 instrumentation amplifier resulted in a small gain but allowed for accurate translation from current to voltage using the internal laser-cut matched resistors as an impedance reference. Unfortunately, low-frequency measurements under 1 kHz did not induce enough current for accurate measurements and high-frequency measurements seemed to introduce significant DC offset error that caused clipping of the negative portion of the signal. Subsequent testing using a transimpedance feedback ladder and a generic high-bandwidth op-amp proved to be too noisy and had a notable DC offset that would have required additional modification to the circuit or post processing for accurate measurements.

The results from these tests drove us to select the Analog Devices AD844 because of its wide flat frequency response and excellent transimpedance characteristics. Initial implementation of the amplifier utilized the feedback ladder, but further investigation proved it to be unnecessary as the AD844 is internally compensated to create a flat frequency response without the need for additional external compensation capacitors. Figure 3.12 shows the simplified TIA schematic and layout without the frequency compensation ladder.

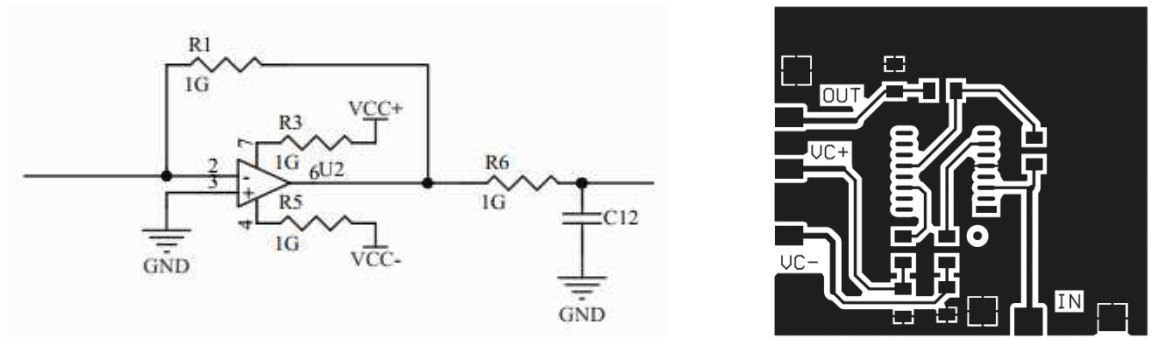

(a) *(b)*

Figure 3.12. *AD844 amplifier circuit (a) and its associated board layout (b).*

This implementation of the TIA circuit utilizes only the AD844, a single 2 kΩ feedback resistor, a decoupling capacitor on each supply rail, and an RC low-pass filter network on the output. The circuit is functional as low as 150 Hz, but additional adjustments to the gain should allow for response down to 10 Hz. The circuit does present some noise, particularly at 25-35 MHz, however, this is beyond the frequency range of our dielectroscopy measurements and can be removed using shielding and the mentioned output RC filter network.

3.4.4 Capacitance Measurements

Although the Solartron 1260A allowed for response measurements using either the PPC or FEF sensor, as a standalone instrument it is unable to measure the capacitance and permittivity properties of a material as provided using the Illionix DSM. These properties are essential to fully characterize the dielectric properties of a material. However, features of the Solartron 1260A have been discovered to achieve capacitance measurements with the addition of the TIA using the existing testbed. To accomplish this, an equation is programmed into the Solartron 1260A to evaluate measurements as they are acquired, and the result is output with respect to frequency. The Solartron is a two-channel differential instrument, thus using one channel to measure the voltage across the sensor and the second to measure the current output as a voltage utilizing the TIA. These measurements can be combined to produce the reactivity, X_C, from which the capacitance can be easily computed. The equation to be programmed into the Solartron 1260A is

$$X_C = \frac{V_1 \cdot R_f}{V_2} \tag{3.14}$$

Where X_C is the reactivity, V_1 is the measured voltage across the sensor, V_2 is the voltage response of the TIA representing the current induced on the sensor, and R_f is the value of the TIA feedback resistor.

$$C = \frac{1}{2\pi f X_C} \tag{3.15}$$

Equation (3.15) can be utilized within Matlab to compute the sample capacitance at each given frequency. C represents our capacitance of interest, X_C is our reactance from (3.14), and f is the frequency the reactance was obtained at, in Hz. Although untested, this configuration in addition to processing in Matlab would provide the complex permittivity in measurements up to 1 MHz and provide similar material property measurements to the Illionix DSM.

Chapter 4. Experimental Results

4.1 BMI Composite Results

4.1.1 Initial BMI Measurements

Measurements utilizing the PPC sensor and initial BMI samples utilized the Illionix DSM and were calibrated by normalizing the measured capacitance vs frequency of each thermally damaged sample against a known undamaged sample measurement. The resultant data, shown in Figure 4.1 demonstrates increasing separation between thermally damaged samples from 50 kHz to 100 kHz with moderate temperature correlation of sample calibrated magnitude at 100 kHz. Low frequency measurements below 1 kHz do not appear to show any correlation with temperature exposure.

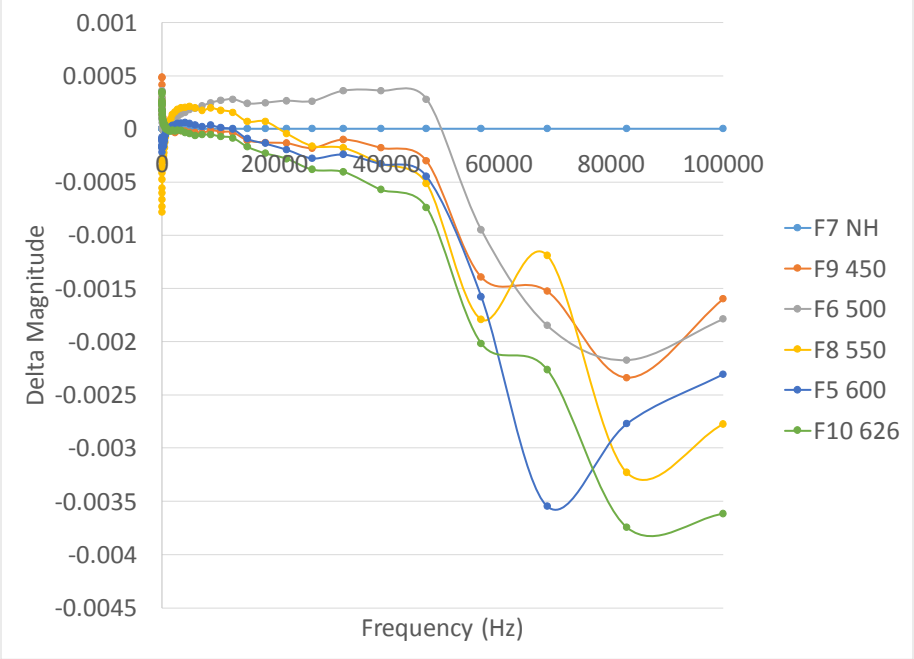

Figure 4.1. *Initial calibrated test measurements using the Illionix DSM demonstrate significant noise and indicate an increasing dielectric response of the material at frequencies exceeding 50 kHz.*

Correlating the capacitance and phase measurements of each sample at 100 kHz results in a transfer function from sensor response to temperature. Figure 4.2 shows the two-variable input

transfer function relative to the exposure temperature of measured samples. Difficulty differentiating between 550□ and 600□ samples prevents perfect temperature correlation, however this function clearly demonstrates identifiable properties and moderately definable thermal damage of 450□, 626□, indicating possible sample identification on the order of 100□. The moderate temperature correlation in gain and phase measurements and increasing separation of sample capacitance measurements at 100 kHz suggests that the BMI samples present increased relaxation response at frequencies above 100 kHz.

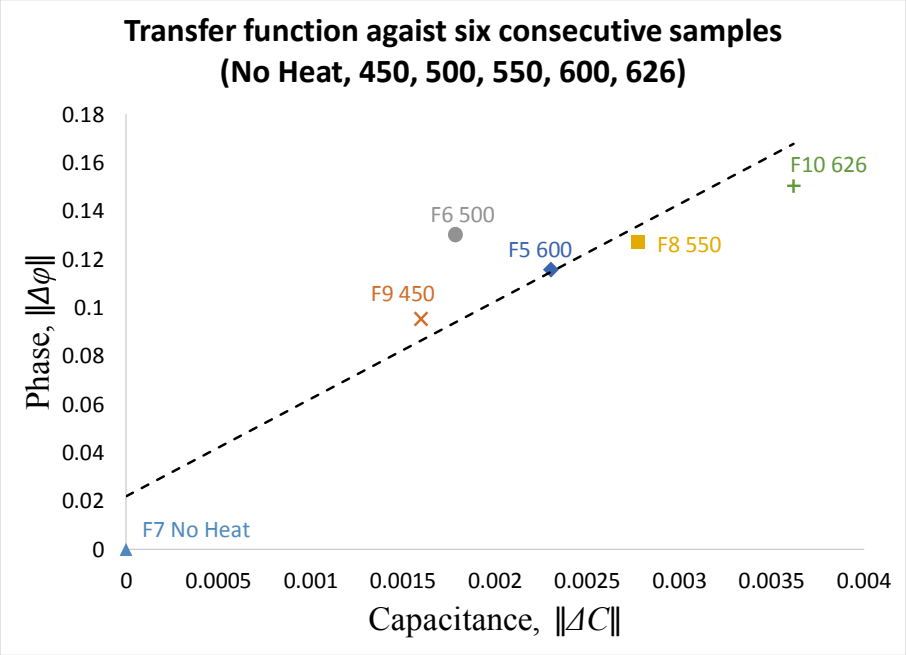

Figure 4.2. *A small signal-to-noise ratio prevents perfect temperature correlation relative to capacitance and phase but indicates higher frequency measurements may yield better sensor response.*

4.1.2 Enhanced Test Configuration BMI Measurements

4.1.2.1 Gain and Phase Temperature Correlation

Measurements using the Solartron 1260A were taken between 10 Hz and 1 MHz with a generator signal voltage of 3 VRMS using the PPC sensor. Three sets of BMI composite samples exposed to temperatures from 425 °F to 600 °F and an undamaged sample were measured fifty times, accumulated, and processed. The accumulated data provides a calibration measurement for

thermal damage identification and, as shown in Figure 4.3, demonstrates a clear delineation of relative thermal damage in the gain and phase response of the sensor. Processed data were plotted using the developed signal processing algorithm described in section 3.2.2. Normalizing the collected data by sample thickness had no impact on the relative plotted ordering of samples by temperature, as such the additional parasitic capacitance due to the air gap above the samples during measurement did not significantly impact the acquired data. Utilizing the processed data, a two-variable input transfer function is created demonstrating direct gain and phase temperature correlation at 1 MHz.

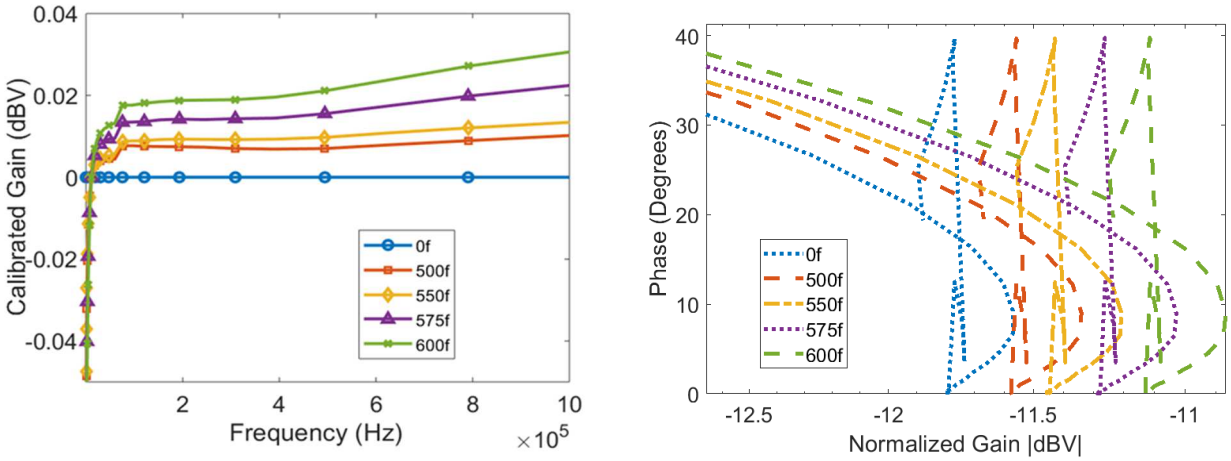

Figure 4.3. *The gain response of averaged sample measurements (a) and phase vs gain response at 1 MHz (b) show perfect temperature correlation and can be clearly identified.*

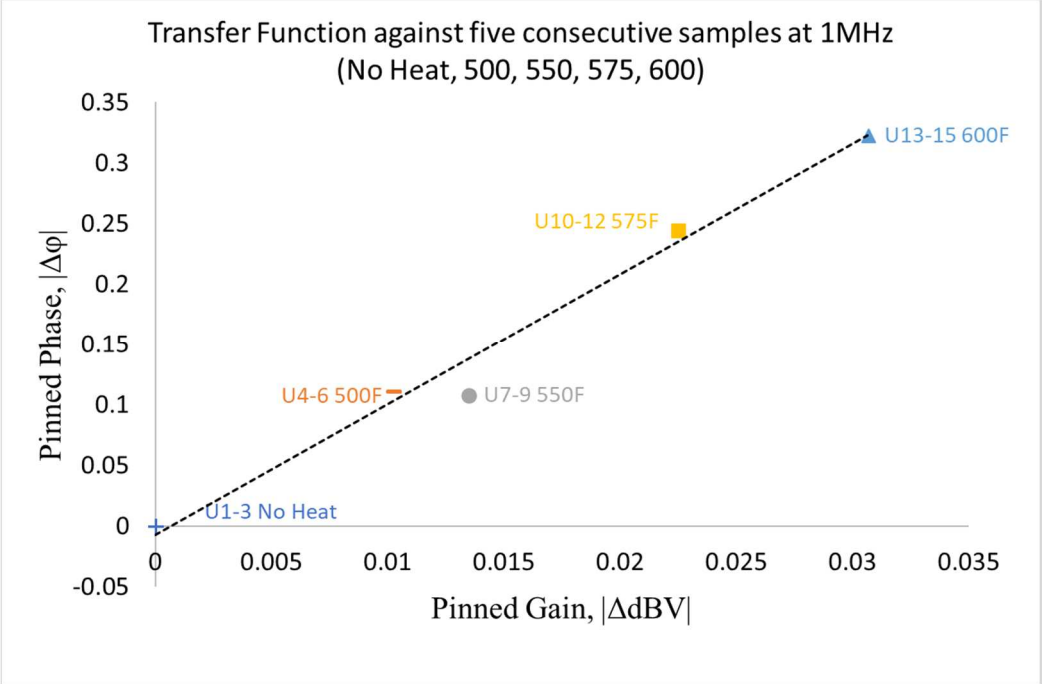

Figure 4.4. *The two-variable input transfer function created using averaged data demonstrates nearly ideal temperature correlation in the phase and gain response.*

The BMI composite has an identifiable response across the entire measured frequency range, with the clearest associations at either end of the spectra. At frequencies below 1 kHz the sensor response between samples is nearly identical, indicating the similarity in the material composition of the samples. At higher frequencies, in excess of 50 kHz, the samples are more easily differentiated, with the most thermally damaged samples demonstrating the greatest gain response. The increased gain response with respect to thermal damage is most likely due to additional cure reactions and hardening of the composite, reducing the mobility of ions in the composite matrix and thus reducing the energy lost as the imaginary part of the complex permittivity.

4.1.2.2 Sample Measurement Error

Although the accumulated test measurements demonstrated nearly perfect temperature correlation, subsequent measurements indicated limited single measurement set repeatability of the temperature correlation. The individual measurements of different thermally exposed samples often overlapped making identification of specific thermal damage difficult. Figure 4.5 shows the

standard deviation from average in the gain response measurements of all samples. Measurement overlap may have been due to several issues including user error during testing, non-visible physical damage to individual samples, and ambient air temperature variation between measurement sets.

There is an additional temperature correlation in the standard deviation which reinforces indications that the chemical structure of the material changes with thermal exposure. The undamaged sample shows the greatest variation in measurement, and its standard deviation overlaps the 500 °F and 550 °F sample measurements. The undamaged sample is likely to be the most structurally flexible and exhibit the least cure reactions resulting in greater molecular mobility. In contrast, the 600 °F samples measure the smallest standard deviation, again indicating a reduction in the mobility of the molecules in the composite matrix with increasing thermal damage.

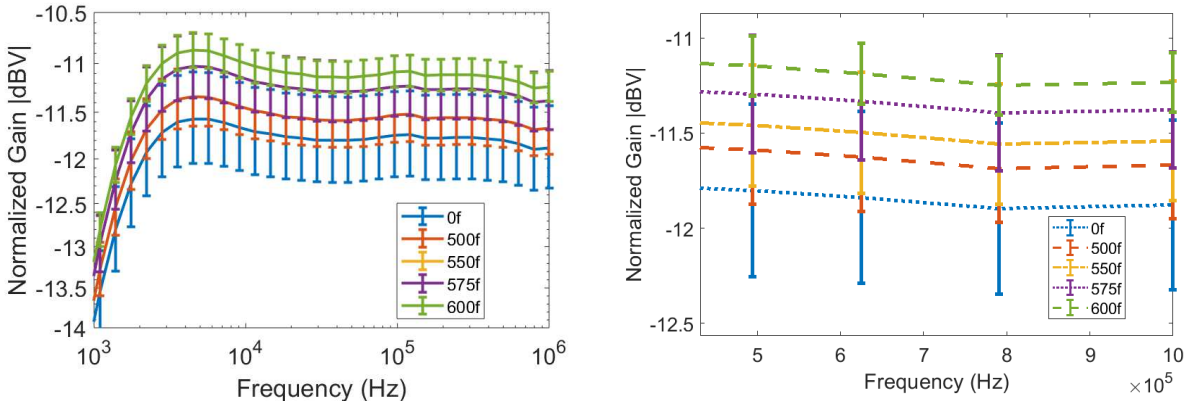

(a) **(b)**

Figure 4.5. *The standard deviation error of sample measurements (a) and zoomed measurements at 1 MHz (b) show a considerable overlap of sample measurements making identification difficult.*

4.1.2.3 Individual Measurement Identification

As a vital part of identifying thermal damage with unknown thermal exposure, five composite samples, exposed to the same thermal damage as the calibration samples, were measured twice and compared to existing data for identification. Utilizing the calibration

measurements as a guideline, Figure 4.6 shows the results in a truth table where the highlighted samples were correctly identified. Of the five samples, only three were correctly and consistently identified, with the undamaged sample proving to be the most difficult to identify from a fixed set of samples. The 575 °F and 600 °F samples were the most easily identifiable, while the 500 °F and 550 °F samples were difficult to differentiate. Once again, this correlates with the standard deviation of samples by exposure. The variation in samples with lower thermal exposure makes their identification more difficult due to overlap in sensor response between samples.

Unknown Identification Table					
	U16	U17	U18	U19	U20
0f	2				
500f			2		
550f				2	
575f					2
600f		2			

Figure 4.6. *Attempted single measurement identification miss identified two of the samples consistently due to significant deviation in sample measurements.*

4.1.3 Identified BMI Sample Properties

4.1.3.1 Intra-sample Variance

Initial testing revealed significant variation in gain and phase sample measurements. Measurements often required repeating or removal during processing due to offset gain error exceeding 20 dB. To identify geometric or physical differences between samples, a full set of geometric data was taken using the PPC and Solartron 1260A. The 500 °F sample was not included during this test because there was no alternate sample at that temperature. The error at lower frequencies is significant with the exception of the 600 °F samples, which likely indicates physical differences between the samples and possibly damage or structure in the composite. High frequency error appears to be flatter, with the undamaged samples exhibiting the least variation

between measurements near 0 dB. The 626□ samples have the largest difference in thickness while the 600°F samples have the smallest, however, these differences in thickness do not translate into measurement error indicating that there does not appear to be a direct correlation between the thickness of the sample and the gain response of the sensor. It is likely that other sources of error in test configuration or sensor configuration impact measurement variation more significantly. The subsequent data is visualized as the measurable difference in dB between samples of the same temperature exposure versus the frequency and is shown in Figure 4.7.

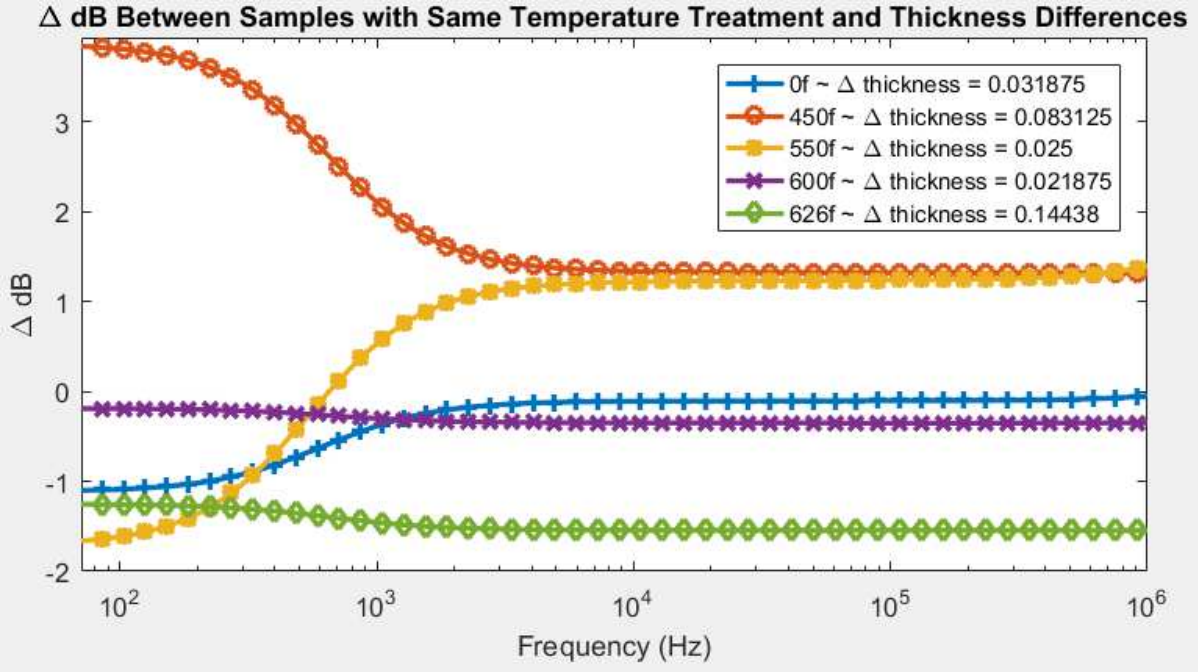

Figure 4.7. *Error between samples of the same temperature exposure without thickness normalization is notably higher at lower frequencies, possibly due to physical damage or structural variation between samples.*

The data in Table 1, Table 2, and Table 3 quantifies the consistency of measurement taken using the mean squared error (MSE) between measurement tests of the same sample. The measurements were taken using the PPC and Solartron 1260A. It is important to note the multiplier in the top left corner of each table indicates that these MSE values are incredibly small, suggesting that test measurements on the same sample with the same orientation are very repeatable, thus this

is reliable data and any variance between tests is indicative of physical damage or some other property of the material.

Table 1: April 5th All Samples Dataset Intra-sample Median MSE

MSE (*10^{-6})	**F1**	**F2**	**F3**	**F4**	**F5**	**F6**	**F7**	**F8**	**F9**	**F10**	**F11**	**F12**
Set 1	N/A	4.15	51.2	8.40	18.8	12.2	9.94	30.4	2.00	13.1	8.98	2.59
Set 2	5.80	3.38	30.8	0.732	3.21	12.8	3.49	9.88	0.493*	8.31	2.90	21.0
Set 3	12.8	5.36	1.42	100	20.5	1.64	50.2	36.5	3.81	1.84	17.0	7.22
Avg	9.32	4.30	27.8	36.6	14.2	8.85	21.2	25.6	2.10*	7.74	9.62	10.3

Table 2: April 9th Small Samples Intra-sample Median MSE

MSE (*10^{-6})	**F2**	**F4**	**F5**	**F7**	**F8**	**F12**
Set 1	57.1	4.77	87.3	309	3.71	11.4
Set 2	99.4	12.5	0.700	31.7	11.8	6.84
Set 3	66.7	9.43	492	N/A	47.9	91.2
Avg	74.4	8.89	193	170*	21.1	36.5

Table 3: April 13th Small Samples Intra-sample Median MSE

MSE (*10^{-6})	**F2**	**F4**	**F5**	**F7**	**F8**	**F12**
Set 1	2.66	1.83	3.11	217	4.86	1.49
Set 2	0.800	5.63	144	18600	0.929	1.27
Set 3	0.657	0.629	0.614	15700	0.486	0.657
Avg	1.37	2.70	49.4	11500	2.09	1.14

4.1.3.2 Geometric Variance

Geometric variance using the FEF sensor is expected to be higher because of the inherent non-linear field lines. To characterize the impact of sample position and the on the sensor geometric test measurements were taken in which each sample was placed on the sensor in a specific position and rotated 90 degrees between test sets. Samples were measured with the sample ID facing up

and the marked edge furthest from the front edge of the shield box. The test configuration is shown in Figure 4.8.

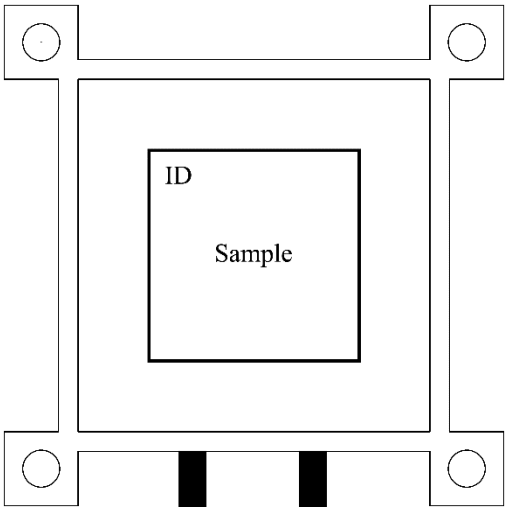

Figure 4.8. *The sample is centered inside the assembly with the identification tag in the top left facing up.*

Using this set up it was observed that the direction of the internal fiber grain relative to the sensor measurably impacted the gain response of the sample being measured. A subset of the smaller samples identified based on the grain orientation was measured to correlate physical orientation with gain and phase measurements. The direction of the fiber was defined as the 45° angle between the sample grain and the edge of the sample opposite the ID marking. An example of the grain orientation and the identified orientation of the samples measured is shown in Figure 4.9 and Table 4 respectively.

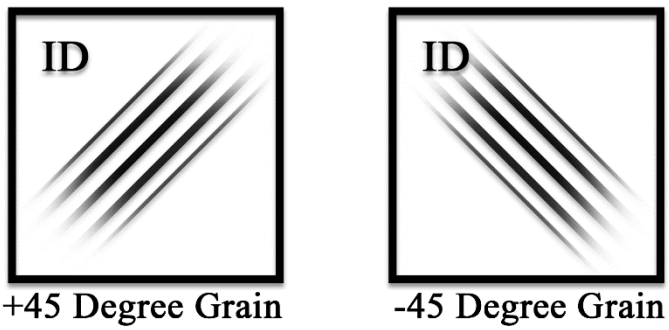

Figure 4.9. *Placing the sample on a Cartesian graph, the direction of the grain dictates the orientation of the sample relative to the marked sample ID.*

Table 4: Small Sample Orientation

Temperature	*Identification*	*Grain Orientation*
No Heat	F7	+45
450F	F12	+45
500F	F2	-45
550F	F8	-45
600F	F5	-45
626F	F4	-45

Measurements of the subset of small samples in Table 4 indicated that rotating a sample by 90 degrees has a significant impact on the relative gain measured. Measurements on all samples showed noticeable variation between rotational test sets. Four of the six samples showed a correlation between the third and first test set measured in both gain and phase response, suggesting that rotating the sample by 180 degrees would achieve similar measurements. Measurement variation in the “no heat” sample and 450□ sample demonstrated up to 1 dB difference in gain as shown in Figure 4.10. These effects are likely due to the non-linear fringing field lines of the sensor and interaction with physical properties of the individual samples such as minor damage or internal structure.

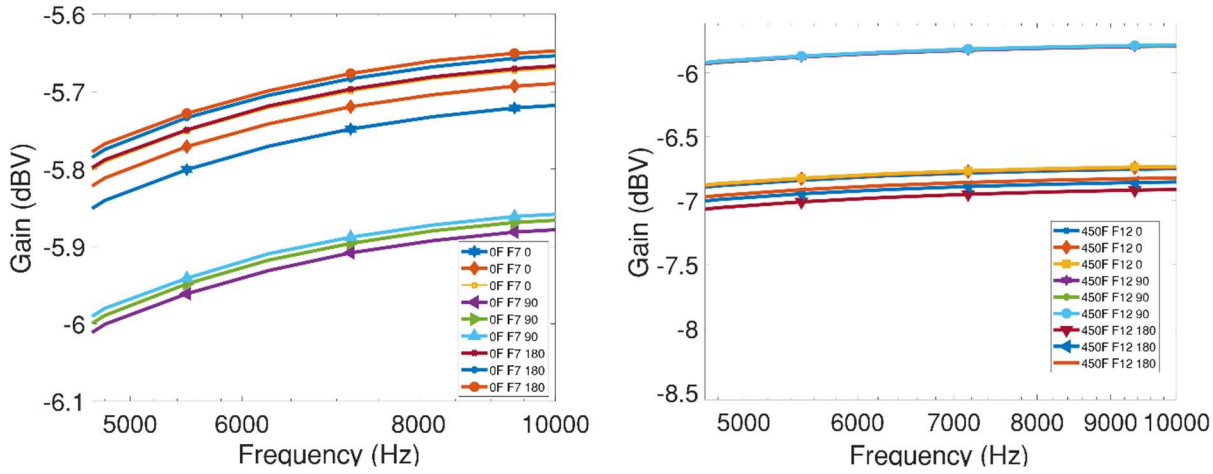

(a) *(b)*

Figure 4.10. *Variance in the F7 "no heat" sample shown as gain separation across three datasets with the higher magnitude datasets measured at 0 and 180 degrees rotation of the sample (a) while the opposite is true of the F12 450□ sample (b).*

4.1.3.3 Sample Surface Finish

Due to the small source of error in within the average test sets using the PPC sensor, any significant variation in measurement of a single sample is most likely due to either non-uniformity of the sample, minor physical damage, or error introduced by the sensor and test configuration. Measurements were plotted as gain vs frequency and phase vs frequency across each location for notable temperature sets. Plots of the raw data for the undamaged sample are shown in Figure 4.11.

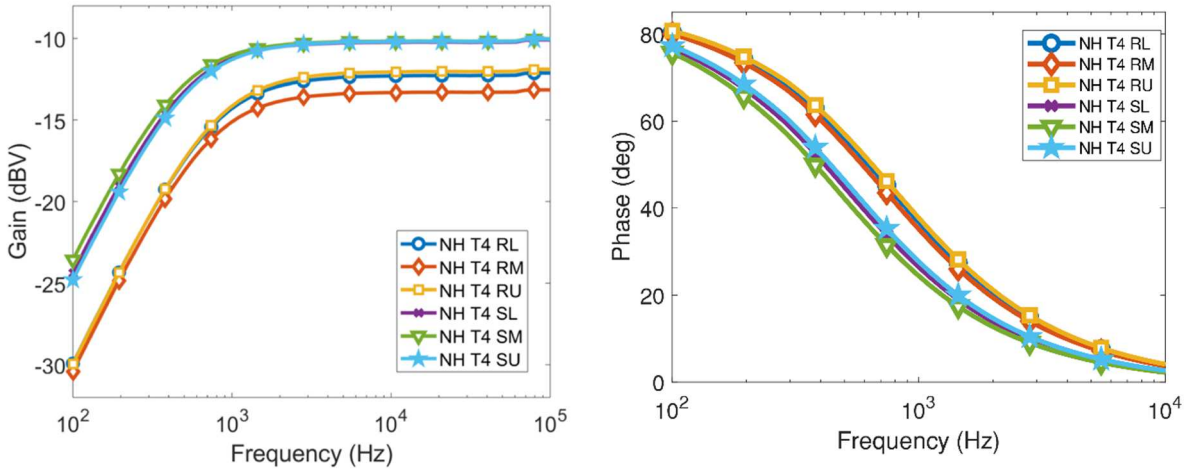

(a) *(b)*

Figure 4.11. *Measurements of the "no heat" sample gain (a) and phase (b) show variation which seems to correlate with the surface finish of the material.*

Measurements on all samples show significant variation between individual measurement locations and in the case of the "no heat" sample indicate a correlation between the surface of the sample facing the sensor and the magnitude response of the sensor. The variation in the measurements is indicative of one of two things: 1) significant variation in the homogeneity of the samples being measured 2) error due to the space created between the sample and the sensor due to the surface finish. Because all samples were cut from the same panel and there is no correlation between specific measured locations on each sample, the effect of surface finish between the sample and sensor is the most probable cause of the variation. Although visually the difference between the rough and smooth sides of the samples is small, at a microscopic level the rough surface appears as a series of mountains and valleys. When the samples are measured with the rough side facing the sensor the uneven surface allows air between the sample and sensor which alters the dielectric response resulting in significant variation in sensor magnitude and phase.

Similar effects plagued the FEF sensor when the rough side of a sample faced the drive and sense electrodes. In the case of the FEF sensor, this issue was reduced by taping plastic wrap to the sensor plate assembly to cover both the drive and sense electrodes. The addition of insulating tape provided a soft surface that reduced the impact of the rough surface of the sample by filling the space between the sensor and sample. To confirm the source of error a layer of plastic wrap

was added to the PPC sensor and an additional measurement set taken to confirm a reduction in the sensor error and determine the impact of the plastic wrap on measurement variance. The raw plotted gain and phase for measurements taken with the "no-heat" undamaged samples demonstrate significantly reduced measurement variance in comparison to prior measurements without an insulated sensor plate.

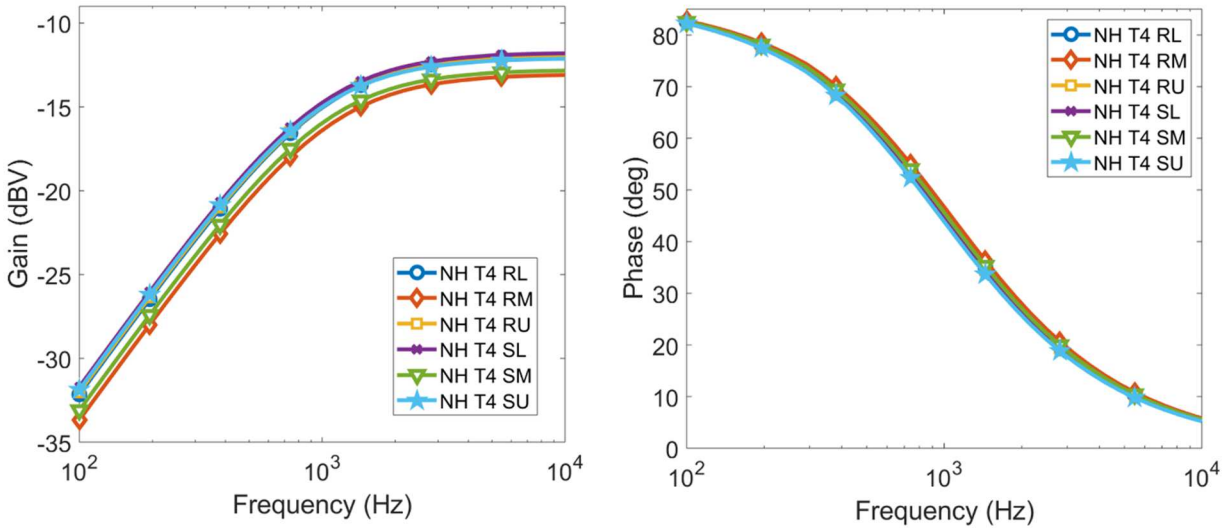

(a) *(b)*

Figure 4.12. *Gain (a) and phase (b) measurements of the "no-heat" sample with the plastic wrap insulating the sensor plate. The reduced measurement variance indicates that sample interaction with the sensor contributed most significantly to measured sample variance.*

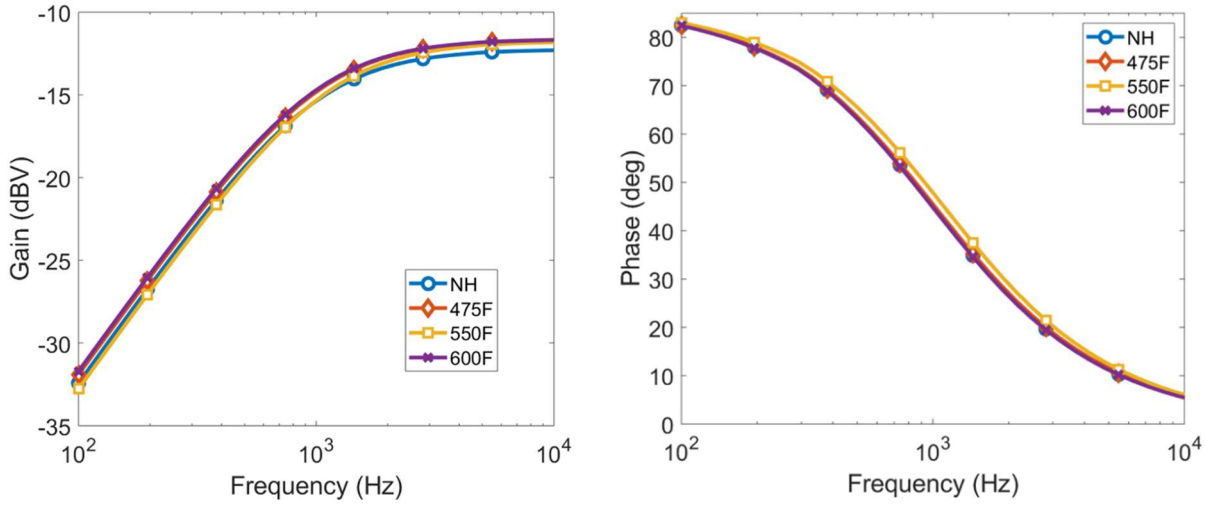

(a) *(b)*

Figure 4.13. *Gain (a) and phase (b) location averages for each sample measured using the insulated sensor show very similar properties and significantly reduced overall variation.*

The plastic wrap used to insulate the sensor wore quickly due to the process of inserting and removing samples from the PPC between test sets. The composite samples were re-measured after covering the sensor plate in a layer of thin packing tape. This provided a more uniform layer of insulation and more consistent test repeatability in comparison to plastic wrap. The combined sample measurements are considerably more uniform than the initial set of measurements and unprocessed measurements show minimal variation in test sets when compared to the non-insulated sensor, indicating more accurate data.

Table 5: Enhanced Sensor Large Sample Variation at 1 MHz

	Tape on Sensor		*No Tape on Sensor*	
Sample Temperature	*Raw Delta Gain*	*Raw Delta Phase*	*Raw Delta Gain*	*Raw Delta Phase*
0□	0.270	0.110	0.977	1.116
475□	0.298	0.143	2.212	0.627
550□	0.371	0.117	1.665	0.357
600□	0.329	0.257	1.584	4.075

4.2 Epoxy Composite Results

4.2.1 Initial Measurements

The epoxy measurements were measured utilizing the enhanced Solartron test configuration in an identical fashion to the BMI samples, with the only difference being a reduction in the gap between electrodes to 4 mm to accommodate the reduced thickness of the epoxy samples. Shown in Figure 4.14, initial epoxy measurements displayed favorable results with the 0□ through 425□ samples demonstrating temperature correlation relative to gain. All samples measured identically up to 1 kHz at which point the corner frequency between the higher temperature samples, 450□ and 475□, measured notably higher gain than all lower temperature samples. Of the lower temperature samples, the 350□ sample is nearly indistinguishable from the undamaged sample measurement while the 400□ and 425□ samples are distinguishable but nearly overlap.

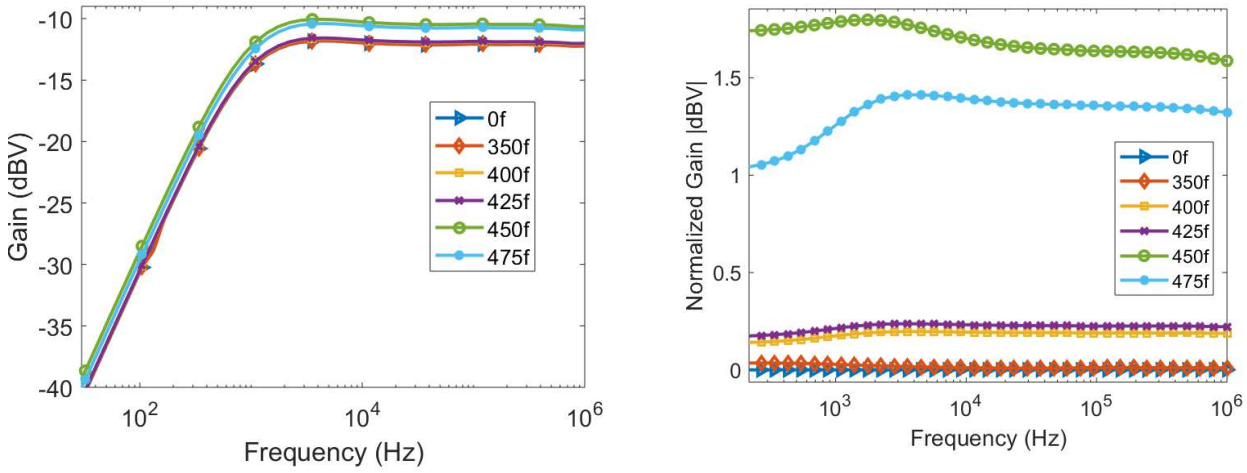

(a) *(b)*

Figure 4.14 *Initial measurement results for the epoxy composite samples both uncalibrated (a) and normalized (b) demonstrating partial temperature correlation and physical damage.*

The increased gain response in the 450□ and 475□ samples is a result of the physical damage of these samples. Shown in Figure 4.15 (a) and (b), the 450□ and 475□ samples have noticeable physical damage in the form of delamination. The voids created by delamination

increase the capacitance, and in relation, the gain response of both samples. Thus, the 450□ sample has the greatest gain response, which correlates with its greater physical damage in comparison to the 475□. The delamination present in both samples is indicative of post incipient thermal damage and can be attributed to weakening of the material and physical or thermal shock following heat exposure.

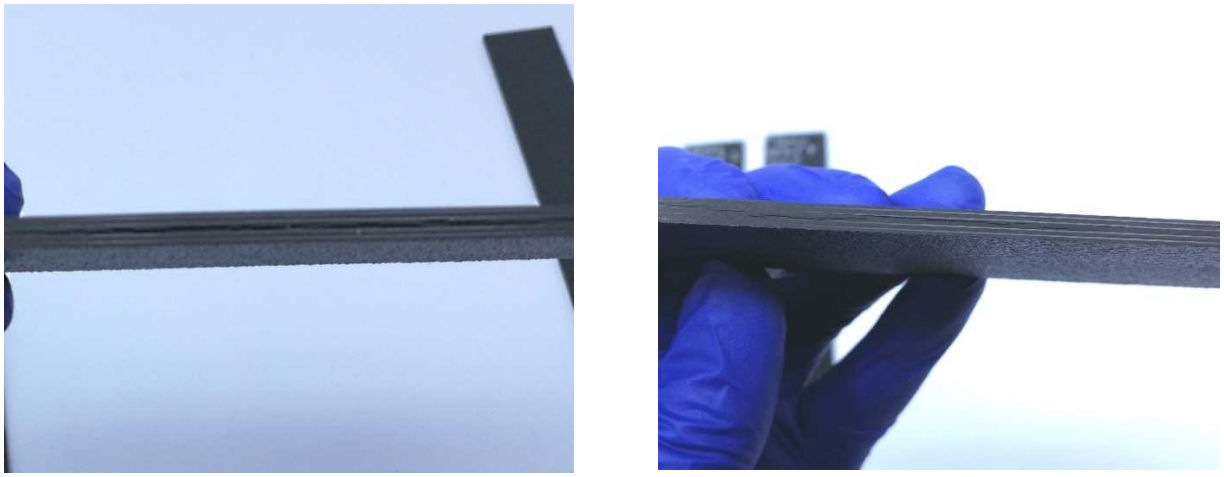

(a) *(b)*

Figure 4.15. *The large difference in measured gain between samples is indicative of physical damage, in this case delamination, which is visible in the 450□ (a) and 475□ (b) samples.*

4.2.2 Measurement Error and Sample Identification

In all measurements taken, relative damage magnitude is identified such that the undamaged sample exhibits the lowest gain measurement and the most damaged samples the greatest. Sample measurement error, shown as the standard deviation in Figure 4.16, is not as considerable as measurements of the BMI composite. However, the mid temperature measurement error overlaps completely, making consistent identification of individual thermal exposure impossible. The 450□ and 475□ samples are clearly identifiable, however relying only on gain measurements it is not possible to isolate the effect of thermal damage from physical damage and the magnitude of these values is likely due to delamination.

Of note is the shift in average value of the 350□ sample. Following initial measurements, the epoxy samples were cut in half to increase the number of measured samples and provide a larger data set for sample identification. All measurements following this procedure demonstrated the overlap and inconsistent temperature correlation in the mid temperature samples shown in Figure 4.16 (b). The increase in gain measurement exhibited by the 350□ is most likely due to physical damage incurred during the cutting procedure while the overlap in the 400□ and 425□ samples is indicative of the limitations of the current sensor relative to thermal resolution.

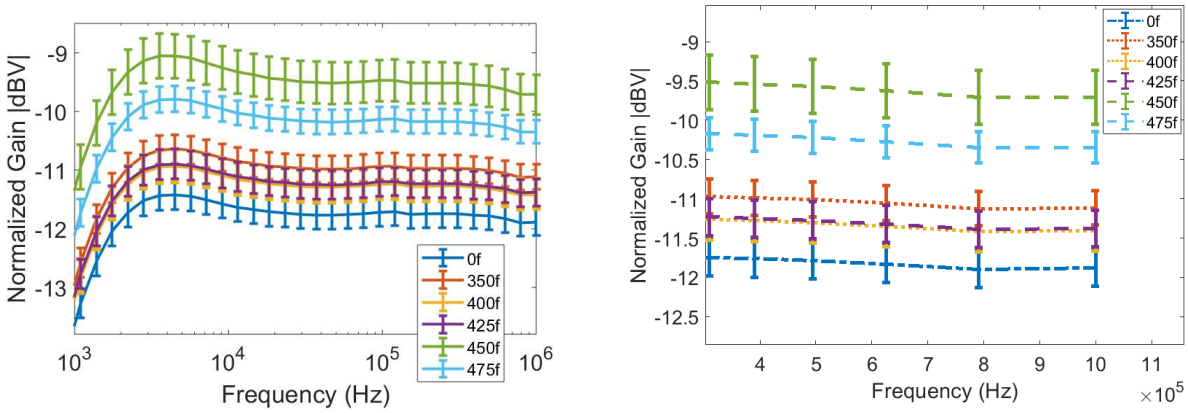

(a) *(b)*

Figure 4.16. *Measurement error of the epoxy samples, shown as the standard deviation in (a) and zoomed in (b) demonstrates overlap making identification difficult.*

Similarly, epoxy composite measurements initially demonstrated temperature exposure correlation above 70 kHz with the exception of the samples with the greatest thermal damage due to physical damage in the form of delamination. For both composites a clear trend of increasing gain response with thermal damage was identified, indicating that thermal exposure of these composites decreases dielectric loss and increases the rigidity of the material. Epoxy composite measurements showed some correlation in temperature but the ability to differentiate between thermal exposures was much lower than in BMI measurements. Unlike the BMI samples, thermal damage is considerably more difficult to quantify in epoxy composite as the relative gain response between thermally exposed samples is much lower and thus measurements often overlapped. In the case of the epoxy composite, the physical damage and delamination of the 450□ and 475□ samples were measurable as a 3 dBV increase in the gain response in comparison to other sample

measurements below 1 kHz. At Higher frequencies, in excess of 50 kHz, the sensor response indicates less dependence of the measured gain on the physical properties of the composites and the differentiation of the samples by thermal exposure increases toward 1 MHz.

Chapter 5. Conclusion and Future Work

5.1 Conclusion

Composite materials are becoming rapidly adopted in aerospace applications due to their light weight and high strength, however existing non-destructive evaluation (NDE) methods used to monitor aircraft integrity are not well suited to examine composite materials. The most common NDE methods, visual inspection, ultrasonic testing and x-ray imaging, focus primarily on visible and physical damage and will only detect cracking, voids, or delamination in composites. Cure reactions in composites caused by heating and aging of the composite matrix considerably reduces the mechanical strength of the material and cannot be detected by these methods. Fourier transform infrared (FTIR) spectroscopy, another NDE method, has been proven to detect damage of this type in composites but is primarily limited to surface measurements and is generally used while removing material to measure at depth, making it impractical for rapid non-destructive evaluation. Electric field sensors can address the challenges with existing composite aircraft NDE methods due to their ability to identify the physical, chemical, and geometric properties of a material. Additionally, multichannel FEF sensor electrodes reside in a single plane allowing for one-sided measurements at various depths into a material making these sensors an ideal choice to rapidly evaluate composite aircraft.

In this thesis we investigated the potential of dielectroscopy via fringing electric field (FEF) sensors to detect incipient thermal damage in bismalemide (BMI) aerospace composites. Two electric field sensors designed to measure composite samples were developed, one in a parallel plate configuration and one as a coplanar FEF sensor. Measurements were obtained by varying the frequency of a sinusoidal potential across the sensors from 10 Hz to 1 MHz and capturing the dielectric response of the composite material under test using a dielectric spectroscopy meter and a gain phase analyzer.

This thesis builds on the NDE of aerospace composites by attempting to detect incipient thermal damage in aerospace BMI CFRP. Existing aerospace NDE methods exclusively detect physical damage in composites and while FTIR spectroscopy capably detects incipient thermal damage, it requires the removal of material to detect damage at depth into the material under test. The results presented herein show that FEF sensors are well suited as an NDE method to evaluate composite aircraft rapidly. Our results indicate that both physical and chemical damage can be detected with these sensors, although discrimination between them would require enhanced calibration and data processing algorithms.

5.2 Future Work

Future work to improve incipient thermal damage detection in aircraft composites can be approached in three ways. First, a multi-channel sensor head supporting discrete wavelengths for detection at specific depths into the material would considerably improve the spatial resolution. The enhanced sensor coupled with further investigation into the effect of physical damage on dielectric gain response and improved sensor shielding would improve measurement reliability. Second, the addition of higher frequency transimpedance circuitry and the integration of capacitance and tan-delta analysis into our processing algorithm. Due to limitations in our test equipment, we lacked the ability to measure capacitance and tan-delta response of the electric field sensors above 100 kHz. The addition of higher frequency transimpedance circuitry or induced current measurement to our testbed would provide more comprehensive dielectric data and allow for more in-depth analysis. These enhancements would improve measurement reliability and more clearly isolate the effects of physical and chemical damage in the MUT. Finally, miniaturization of the measurement equipment would allow for practical application of this technology in evaluating composite aircraft.

Bibliography

[1] K. Sundara-Rajan, L. Byrd, and A. V. Mamishev, "Moisture content estimation in paper pulp using fringing field impedance Spectroscopy," *Ieee Sensors Journal,* vol. 4, no. 3, pp. 378-383, Jun 2004, doi: 10.1109/jsen.2004.824230.

[2] M. C. Hegg, A. Ogale, A. Mescher, A. V. Mamishev, and B. Minaie, "Remote Monitoring of Resin Transfer Molding Processes by Distributed Dielectric Sensors," *Journal of Composite Materials,* vol. 39, no. 17, pp. 1519-1539, 2005, doi: 10.1177/0021998305051083.

[3] H. C. Wang, A. Zyuzin, and A. V. Mamishev, "Measurement of Coating Thickness and Loading Using Concentric Fringing Electric Field Sensors," *Ieee Sensors Journal,* vol. 14, no. 1, pp. 68-78, Jan 2014, doi: 10.1109/jsen.2013.2279991.

[4] R. H. Bhuiyan, R. A. Dougal, and M. Ali, "Proximity coupled interdigitated sensors to detect insulation damage in power system cables," (in English), *Ieee Sensors Journal,* Article vol. 7, no. 11-12, pp. 1589-1596, Nov-Dec 2007, doi: 10.1109/jsen.2007.908440.

[5] S. Dian, M. Liang, B. Lou, and T. Liu, "A novel FEF method for insulation status monitoring of underground power cables," *Journal of Computers (Finland),* vol. 8, no. 2, pp. 441-447, 2013, doi: 10.4304/jcp.8.2.441-447.

[6] J. W. Gardner *et al.*, "Integrated array sensor for detecting organic solvents," *Sensors and Actuators, B: Chemical,* vol. B26, no. 1 -3 pt 1, pp. 135-139, 1995.

[7] E. S. Kolesar Jr and J. M. Wiseman, "Interdigitated gate electrode field effect transistor for the selective detection of nitrogen dioxide and diisopropyl methylphosphonate," *Analytical Chemistry,* vol. 61, no. 21, pp. 2355-2361, 1989.

[8] X. B. B. Li, S. D. Larson, A. S. Zyuzin, and A. V. Mamishev, "Design principles for multicuhannel fringing electric field sensors," *Ieee Sensors Journal,* vol. 6, no. 2, pp. 434-440, Apr 2006, doi: 10.1109/jsen.2006.870161.

[9] X. B. Li, G. Rowe, V. Inclan, and A. V. Mamishev, "Nondimensionalized parametric modeling of fringing efectric-field sensors," *Ieee Sensors Journal,* vol. 6, no. 6, pp. 1602-1608, Dec 2006, doi: 10.1109/jsen.2006.883861.

[10] K. J. Andrew, "Dielectric relaxation in solids," vol. 32, ed, 1999, pp. R57-R70.

[11] J. Jiao, L. Li, B. Wu, and C. He, "Novel capacitive proximity sensors for assessing the aging of composite insulators," *Sensors and Actuators a-Physical,* vol. 253, pp. 75-84, Jan 1 2017, doi: 10.1016/j.sna.2016.11.025.

[12] Y. Ye, J. Deng, S. Shen, Z. Hou, and Y. Liu, "A Novel Method for Proximity Detection of Moving Targets Using a Large-Scale Planar Capacitive Sensor System," *Sensors,* vol. 16, no. 5, May 2016, Art no. 699, doi: 10.3390/s16050699.

[13] W. Wang, W. Wang, and Z. Liu, "Investigation of displacement measurement method based on fringing field capacitor," *Iet Science Measurement & Technology,* vol. 11, no. 1, pp. 63-66, Jan 2017, doi: 10.1049/iet-smt.2016.0187.

[14] P. F. Laleicke and F. A. Kamke, "A capacitive multi-wavelength sensor for moisture content gradient sensing in wood," *Wood Science and Technology,* vol. 52, no. 3, pp. 717-732, May 2018, doi: 10.1007/s00226-018-0988-z.

[15] A. I. Zia, S. C. Mukhopadhyay, P.-L. Yu, I. H. Al-Bahadly, C. P. Gooneratne, and J. Kosel, "Rapid and molecular selective electrochemical sensing of phthalates in aqueous solution," *Biosensors & Bioelectronics,* vol. 67, pp. 342-349, May 15 2015, doi: 10.1016/j.bios.2014.08.050.

[16] A. Henning *et al.*, "Control of the Intrinsic Sensor Response to Volatile Organic Compounds with Fringing Electric Fields," *Acs Sensors,* vol. 3, no. 1, pp. 128-134, Jan 2018, doi: 10.1021/acssensors.7b00754.

[17] A. Risos, N. Long, and G. Gouws, "A temperature compensated dielectric test cell for accurately measuring the complex permittivity of liquids," *Review of Scientific Instruments,* vol. 88, no. 10, Oct 2017, Art no. 105105, doi: 10.1063/1.5005857.

[18] C. Daily, "Dielectric properties and degradation monitoring in polymer-matrix structural composites," N. Bowler, S. Beckman, V. Dayal, R. Roberts, and X. Tan, Eds., ed: ProQuest Dissertations Publishing, 2015.

[19] A. Risos, N. Long, A. Hunze, and G. Gouws, "Interdigitated Sensors: A Design Principle for Accurately Measuring the Permittivity of Industrial Oils," *Ieee Sensors Journal,* vol. 17, no. 19, pp. 6232-6239, Oct 1 2017, doi: 10.1109/jsen.2017.2732942.

[20] A. Risos, "Interdigitated Sensors: The Next Generation "Sensing Permittivity and Conductivity of Oils - Unaffected by Temperature"," *Ieee Sensors Journal,* vol. 18, no. 9, pp. 3661-3668, May 1 2018, doi: 10.1109/jsen.2018.2810827.

[21] A. Risos and G. Gouws, "In-situ aging monitoring of transformer oil via the relative permittivity and DC conductivity using novel interdigitated dielectrometry sensors (IDS)," *Sensors and Actuators B-Chemical,* vol. 287, pp. 602-610, May 15 2019, doi: 10.1016/j.snb.2018.12.037.

[22] N. Li, X. D. Yang, Y. Gong, and P. Wang, "Enhancing electrical capacitance tomographic sensor design using fuzzy theory based quantifiers," (in English), *Measurement Science and Technology,* Article vol. 25, no. 12, p. 10, Dec 2014, Art no. 125401, doi: 10.1088/0957-0233/25/12/125401.

[23] X. Yin, D. A Hutchins, G. Chen, and W. Li, *Investigations into the measurement sensitivity distribution of coplanar capacitive imaging probes*. 2013, pp. 1-9.

[24] X. Yin, D. A. Hutchins, G. Chen, and W. Li, "Preliminary studies on the design principles of capacitive imaging probes for non-destructive evaluation," *International Journal of Applied Electromagnetics and Mechanics,* vol. 42, no. 3, pp. 447-470, 2013 2013, doi: 10.3233/jae-131676.

[25] K. Wang, X. Yin, C. Li, W. Li, and G. Chen, "Capacitive Imaging Technique for the Inspection of Composite Sucker Rod," *Chinese Journal of Mechanical Engineering,* vol. 32, no. 1, Dec 5 2019, Art no. 105, doi: 10.1186/s10033-019-0421-z.

[26] S. Gholizadeh, "A review of non-destructive testing methods of composite materials," *Procedia Structural Integrity,* vol. 1, pp. 50-57, 2016, doi: 10.1016/j.prostr.2016.02.008.

[27] E. Drukker, A. K. Green, and G. Marom, "Mechanical and chemical consequences of through thickness thermal gradients in polyimide matrix composite materials. Composites Part A " *Applied Science and Manufacturing, ,* vol. 34, no. 2, pp. 125-133, February 2003.

[28] Odegard G.M. and Bandyopadhyay. A., "Physical Aging of Epoxy Polymers and Their Composites, Journal of Polymer Science Part B," *Polymer Physics,* vol. 49, no. 24, pp. 1695□1716, 2011.

[29] D. Lévêque, . , H. Katoh, J. Cinquin, and K. Hasegawa, "Durability evaluation of carbon/bmi composites after thermal aging, ," in *18th International Conference on Composite Materials (ICCM18)*, August 21- 26, 2011.

[30] G. Marina and R. Chartoff, "High Temperature Stability of Advanced Thermosetting Resin Based Composite," in *13th International Conference on Composite Materials (ICCM13)* June 2001.

[31] V. M. Karbhari, *Non-destructive evaluation (nde) of polymer matrix composites techniques and applications* (Woodhead Publishing Series in Composites Science and Engineering). Philadelphia, PA: Philadelphia, PA : Woodhead Pub., 2013.

[32] Z. Qu, P. Jiang, and W. Zhang, "Development and Application of Infrared Thermography Non-Destructive Testing Techniques," *Sensors (Basel, Switzerland),* vol. 20, no. 14, p. 3851, 2020, doi: 10.3390/s20143851.

[33] F. Ciampa, P. Mahmoodi, F. Pinto, and M. Meo, "Recent Advances in Active Infrared Thermography for Non-Destructive Testing of Aerospace Components," *Sensors (Basel, Switzerland),* vol. 18, no. 2, p. 609, 2018, doi: 10.3390/s18020609.

[34] T. Howie, A. Tracey, D. Pate, J. Morasch, and B. Flinn, "The Detection of Incipient Thermal Damage of CFRP Using FTIR," in *SAMPE technical conference proceedings*, 2014.

[35] T. Howie, A. Tracey, P. Vahey, P. Shelley, and B. Flinn, "Handheld FTIR Guided Repair of CFRP Composite with Localized Incipient Thermal Damage," in *CAMX conference proceedings* 2014.

[36] T. Howie, A. Tracey, and B. Flinn, "Composite Thermal Damage Measurement with Handheld Fourier Transform Infrared Spectroscopy," in *FAA report DOT/FAA/TC-15/51*, January, 2016.

[37] R. Toivola, F. Afkhami, S. Baker, J. McClure, and B. D. Flinn, "Detection of incipient thermal damage in carbon fiber-bismaleimide composites using hand-held FTIR," *Polymer Testing,* vol. 69, pp. 490-498, Aug 2018, doi: 10.1016/j.polymertesting.2018.05.036.

[38] R. Richert, "A simple current-to-voltage interface for dielectric relaxation measurements in the range 10(-3) to 10(7) Hz," (in English), *Review of Scientific Instruments,* Article vol. 67, no. 9, pp. 3217-3221, Sep 1996, doi: 10.1063/1.1147445.